SANDIA REPORT
SAND2007-0835
Unlimited Release
Printed March 2007

Advanced Diagnostics for Impact-Flash Spectroscopy on Light-Gas Guns

Michael C. Wanke, Albert D. Grine, Mike A. Mangan Lalit C. Chhabildas, William D. Reinhart, Tom F. Thornhill, C. Scott Alexander, Justin L. Brown, William G. Breiland, Eric A. Shaner, Paul A. Miller

Prepared by
Sandia National Laboratories
Albuquerque, New Mexico 87185 and Livermore, California 94550

Sandia is a multiprogram laboratory operated by Sandia Corporation,
a Lockheed Martin Company, for the United States Department of Energy's
National Nuclear Security Administration under Contract DE-AC04-94AL85000.

Approved for public release; further dissemination unlimited.

Issued by Sandia National Laboratories, operated for the United States Department of Energy by Sandia Corporation.

NOTICE: This report was prepared as an account of work sponsored by an agency of the United States Government. Neither the United States Government, nor any agency thereof, nor any of their employees, nor any of their contractors, subcontractors, or their employees, make any warranty, express or implied, or assume any legal liability or responsibility for the accuracy, completeness, or usefulness of any information, apparatus, product, or process disclosed, or represent that its use would not infringe privately owned rights. Reference herein to any specific commercial product, process, or service by trade name, trademark, manufacturer, or otherwise, does not necessarily constitute or imply its endorsement, recommendation, or favoring by the United States Government, any agency thereof, or any of their contractors or subcontractors. The views and opinions expressed herein do not necessarily state or reflect those of the United States Government, any agency thereof, or any of their contractors.

Printed in the United States of America. This report has been reproduced directly from the best available copy.

Available to DOE and DOE contractors from
U.S. Department of Energy
Office of Scientific and Technical Information
P.O. Box 62
Oak Ridge, TN 37831

Telephone: (865) 576-8401
Facsimile: (865) 576-5728
E-Mail: reports@adonis.osti.gov
Online ordering: http://www.osti.gov/bridge

Available to the public from
U.S. Department of Commerce
National Technical Information Service
5285 Port Royal Rd.
Springfield, VA 22161

Telephone: (800) 553-6847
Facsimile: (703) 605-6900
E-Mail: orders@ntis.fedworld.gov
Online order: http://www.ntis.gov/help/ordermethods.asp?loc=7-4-0#online

SAND2007-0835
Unlimited Release
March 2007

Advanced Diagnostics for Impact-Flash Spectroscopy on Light-Gas Guns

Michael C. Wanke, Albert D. Grine, and Mike A. Mangan
Photonics Microsystems Technologies Department

Lalit C. Chhabildas, William D. Reinhart, Tom F. Thornhill,
C. Scott Alexander, and Justin L. Brown
Solid Dynamics and Energetic Materials Department

William G. Breiland
Mission Analysis & Simulation Department

Eric A. Shaner
Semiconductor Materials and Device Sciences Department

Paul A. Miller
Laser, Optics & Remote Sensing Department

P.O. Box 5800
Albuquerque, New Mexico 87185-MS1181

ABSTRACT

This study is best characterized as new technology development for implementing new sensors to investigate the optical characteristics of a rapidly expanding debris cloud resulting from hypervelocity impact regimes of 7 to 11 km/s. Our gas guns constitute a unique test bed that match operational conditions relevant to hypervelocity impact encountered in space engagements. We have demonstrated the use of (1) terahertz sensors, (2) silicon diodes for visible regimes, (3) germanium and InGaAs sensors for the near infrared regimes, and (4) the Sandia lightning detectors which are similar to the silicon diodes described in 2. The combination and complementary use of all these techniques has the strong potential of "thermally" characterizing the time-dependent behavior of the radiating debris cloud. Complementary spectroscopic measurements provide temperature estimates of the impact generated debris by fitting its spectrum to a blackbody radiation function. This debris is time-dependent as its transport/expansion behavior is changing with time. The rapid expansion behavior of the debris "cools" the cloud rapidly, changing its thermal/temperature characteristics with time. A variety of sensors that span over a wide spectrum, varying from visible regime to THz frequencies, now gives us the potential to cover the impact over a broader temporal regime starting from high-pressures (Mbar) high-temperatures (eV) to low pressures (mbar) low temperatures (less than room temperature) as the debris expands and cools.

EXECUTIVE SUMMARY

This study may be best characterized as new technology development which can lead to the implementation of new sensors for use in investigating the optical characteristics of a rapidly expanding debris cloud that result from hypervelocity impact. In particular, this project expanded the diagnostics for dynamic spectroscopy at our gas-gun facility from the visible and infrared into the THz region of the spectrum. Our gas guns constitute a unique test bed that provides well-controlled experimental environments that match operational conditions relevant to hypervelocity impact such as those encountered in space engagements.

Extending our impact-flash spectral measurements into the THz regime allowed us to perform tests and analysis in this new spectral regime, which is complementary to our current capabilities in the visible and infrared. THz spectroscopy may potentially offer significant advantages, in particular, the THz region is less crowded, and will still be emitted by molecules that have cooled too much to emit in the infrared. THz spectra relate to molecular motions, some of which have been cataloged for operational materials of interest. The combined capabilities would offer a much broader range of material identification possibilities and complement/verify those achievable with the atomic measurements provided by visible and infrared spectroscopy alone. More significantly, these combined technologies now have the potential of identifying the dissociation or reaction products of many systems that has undergone a high velocity impact and deformation. To begin exploring the usefulness of applying THz technology to understand impact phenomenology, this LDRD effort provided new measurement and recording systems appropriate for THz investigations in these dynamic environments. In addition, we further enhanced existing visible and near-infrared capabilities.

This study also complemented the spectroscopic measurements by obtaining temperature estimates of the impact generated debris that results from high velocity engagements. The impact generated debris is time-dependent in that its transport/expansion behavior is changing with time. The rapid expansion behavior of the debris is expected to “cool” the cloud rapidly, thus changing its thermal characteristics with time. The test methodology consisted of fitting the debris emission spectrum to a blackbody radiation function even though the debris cloud may not be in thermodynamic equilibrium.

In this study we have implemented new sensors for use in investigating the optical characteristics of a rapidly expanding debris cloud that results from hypervelocity impact. We have demonstrated the use of (1) terahertz sensors, (2) silicon diodes for visible regimes, (3) germanium and InGaAs sensors for the near infrared regimes, and (4) the Sandia lightning detectors which are similar to the silicon diodes described in 2. The combination and complementary use of all these techniques has the strong potential of “thermally” characterizing the time-dependent behavior of the radiating debris cloud.

A variety of sensors that span over a wide spectrum, varying from visible regime to THz frequencies, now gives us the potential to cover the impact over a broader temporal regime starting from high-pressures (Mbar) high-temperatures (eV) to low pressures (mbar) low temperature (less than room

temperature) as the debris expands and cools. In addition the broad frequency coverage enables one to improve determination of the cloud constituents and dynamics by exploring multiple phenomenology. The output signatures of many of these sensors are summarized in this report. Results from some of these sensors are also described.

ACKNOWLEDGMENTS

Thanks to Heidi Anderson and John Martinez for their enthusiastic experimental support during this study.

CONTENTS

FIGURES

TABLES

1. INTRODUCTION

We have demonstrated impact-flash spectroscopy operating in the visible and near-infrared (NIR) as a credible technology. This real time diagnostic tool provides assessment of high velocity impacts that result in high-engagement temperatures and pressures where atomic emissions dominate the impact flash signatures. Terahertz (THz) frequency spectra will extend these capabilities to later times when lower temperatures and pressures are present.

The principle and the motivation for extending these capabilities into the THz regime are summarized as follows. The THz region of the electromagnetic spectrum may be the best frequency range for high confidence, high specificity material detection because many molecules, from simple diatomic chemicals to complex macromolecules have stronger and more distinctive absorption and emission resonances at THz frequencies than in either microwave or near infrared to visible ranges. This provides significantly enhanced spectral resolution in contrast to infrared signatures.

One of the key advantages of THz spectroscopy is that analysis of the rotational constants of molecules can be performed using fundamental quantum mechanics theories. With these measured rotational constants, an absolute identification of the molecule, both qualitatively and quantitatively, can be made. In most cases of interest, molecular absorption and emission cross sections are also very large in the THz range, leading to potentially excellent signal to noise ratios for detection, and thus high sensitivity to small concentrations. As an example, at 1 THz, the rotational energy transitions are comparable to a thermal energy of only ~50K. Molecules above this temperature will both emit as well as absorb at rotational transitions at or below 1 THz. Thus, for gas molecules at a temperature higher than the background temperature, the characteristic spectral features can be easily observed using only passive detection. Also, the emission flux from a fixed number of molecules is a strong function of temperature, which can be significant for high velocity impact engagements. These advantages of the THz frequency range allow for enormous potential in the areas of remote spectroscopy with an unprecedented level of discrimination, sensitivity, and accuracy.

The intent of this project was to begin extending our impact-flash spectral measurements into the THz regime to allow us to perform tests and analysis in this new spectral region. These techniques complement existing capabilities in the visible and infrared allowing a full suite of detectable frequencies. In particular, the THz region is less “crowded” spectrally, and will still be emitted by molecules that are too cool to emit in the infrared, and may not have detectable spectra in the visible. Our goal in this project was to observe THz emission from impact debris, to provide estimates of the emission intensity, and to observe molecular signatures from the impact generated cloud. As part of this work, we expanded the diagnostics for dynamic

spectroscopy at our gas-gun facility in the visible and infrared and in the THz region, to more effectively understand the operational requirements relevant to high velocities impacts.

Even though the report emphasizes the terahertz technology, we have also demonstrated the use of broad band diodes both in the visible and infrared regimes. This has successfully allowed us to characterize the time-dependent behavior of the radiating debris. In summary, we have successfully expanded the use of new techniques to characterize the radiating and expanding debris cloud that results from hypervelocity impact engagements. Results of this study maybe highlighted as follows:

1. THz emission from impact debris has been successfully demonstrated.
2. Silicon diodes can be used in the visible regime both in a broad band regime or as a narrow band spectrometer at specific wavelengths to determine its time-dependent radiation emission with nanosecond time resolution.
3. Silicon diode measurements at four specific wavelengths have been used as a pyrometer to estimate the temperature of the expanding and radiating hypervelocity impact-generated debris.
4. Temperature estimates are also determined using the results of optical emission data recorded by the multi-channel analyzer both in the visible and near infra-red regime.
5. Temperature estimates for Comp-B are much higher than expected or estimated based on the assumption that the debris cloud is expanding as an ideal gas.
6. Sandia lightning detectors were also used in some experiments to measure the broad band radiation in the visible regime. It is not unlike the silicon diodes in that it had a “larger” detection area compared to the silicon diode mentioned above with the sampling rate of a microsecond.

2. EXPERIMENT DESIGN

2.1. Target Choice

Well after an impact event in a low pressure environment the pressures in the expanding and radiating debris are relatively low. At these pressures THz signatures of many molecules are very unique, enabling identification even with only a few spectral lines over a narrow spectral region. In such cases the emission lines can be quite narrow and may be closely spaced. Thus high resolution spectroscopy is desirable to take full advantage of the available signatures. For ultimate detection specificity, high-resolution heterodyne detection covering the frequency intervals of the expected signatures would be desired. Unfortunately, a heterodyne detector with the speed and bandwidth required was not obtainable for this project.

Therefore we planned to measure the THz signatures with a detector being developed under a separate LDRD. It exhibits a fast, tunable, narrow-band spectroscopic response with a resolution around 40 GHz, but does not have the highest sensitivity. Given these limitations we wanted a target possessing a large cross-section and spectral lines separated by more than 40 GHz. Water vapor is known to fit these criteria well but is not an ideal target material. Instead we realized we could be synergistic with other experiments using Comp-B as a target since the major byproducts of most explosives are H2O, CO, CO2, and N2. CO2 and N2 do not have permanent dipole moments since they are centro-symmetric molecules and therefore have negligible rotational spectra. Thus the major spectral lines of Comp-B should be dominated by water spectra which are ideally suited for proof-of-principle testing.

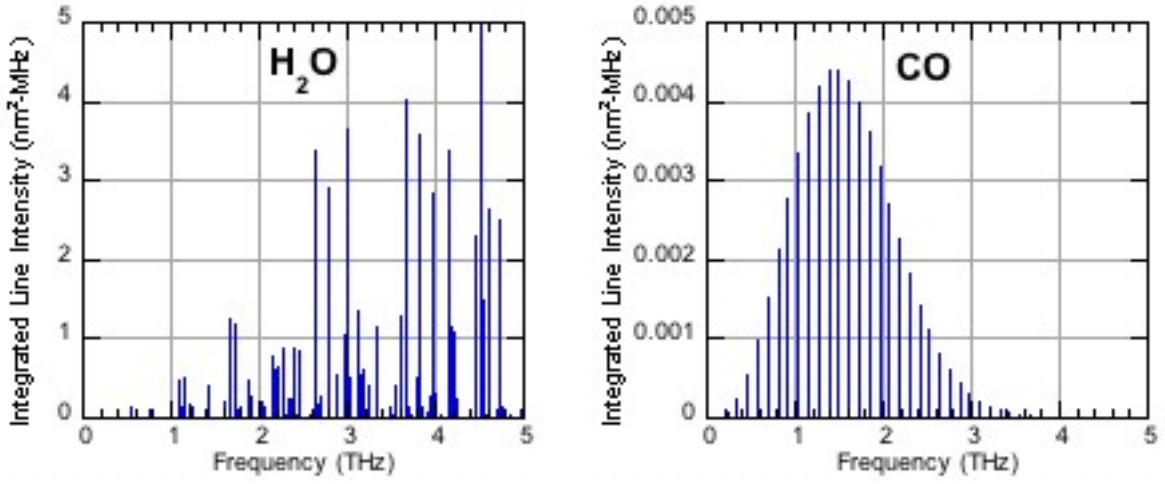

Figure 1. Spectral integrated line intensities of H_2O, and CO at a temperature of 300K. (Taken from the JPL database at http://spec.jpl.nasa.gov)

Therefore we chose Comp-B to be our target material. Its actual detonation by-products are listed in Table 1 and water vapor is the most prevalent [1]. Therefore, even though there will be many different molecular species (some with unknown spectra), the water vapor lines should dominate. In addition to being synergistic with other work it also has the advantage of being a solid at room temperature making target handling easier.

Table 1. Detonation By-Products of Comp-B Computed Using CHEETAH

Comp-B detonation by-products			
By-Product	*Mol/kg*	*% in Mixture*	*Lnfl id#*
H_2O	12.48	39.7452229299	1
N_2	10.74	34.2038216561	22
CO2	6.089	19.3917197452	2
CO	2.078	6.6178343949	5
CH_2O_2	0.01438	0.0457961783	X
NO	0.005885	0.0187420382	8
CH_4	0.002952	0.0094012739	6
C_2H_4	0.001919	0.006111465	38
H_2	0.00104	0.0033121019	X
O_2	0.000677	0.002156051	7
CH_3OH	0.0004866	0.0015496815	X
H_3N	0.000276	0.00087898	X
CH_2O	0.00002004	0.0000638217	20
CH_3	3.05e-008	9.72e-008	0.0
C_2H_6	1.1e-009	3.6e-009	27
NO_2	0.0	0.0	10
Total mols gas	31.415		

2.2. Expected Emissions

In order to design the detection set-up, we needed an estimate of the power emitted per line. There are many uncertainties in the measurements so some simplifying assumptions are made regarding the temperature, pressure, and make-up of the target by-products. To calculate the emission from the gas we took the following steps, each of which will be subsequently described in more detail.

- Determined the chemical by-products of Comp-B using CHEETAH.
- Calculated the temperature, pressure and volume of the cloud using the equation of state for an ideal gas expanding into a vacuum.

- Calculated the absorption per unit length of the by-products using a line-by-line radiation transfer model in conjunction with the HITRAN spectroscopic database for a specific temperatures and pressures.

- Calculated the absorption through the column of gas defined by the detection optics by multiplying the path length by the absorption per unit length.

- And finally calculated the emission by setting the emissivity equal to the absorptivity, by assuming that the gas was in quasi-static equilibrium such that Kirchhoff's law applied, and thus treated the cloud as a graybody [1].

2.2.1 Calculating Temperature Pressure and Volume: Equation of State

In the following we present a notional analysis of the gas cloud generated by a fast-moving Lexan projectile hitting a stationary target consisting of explosive (comp B) that is detonated by the collision. This is a very simplified analysis. Although the debris cloud probably contains a spray of liquid and solid particles, this analysis addressed only gas dynamics. We first determine the initial energy in the gas cloud and, subsequently, examine the dynamics of the gas cloud.

Kinetics and Energy

In this section, we examine collision dynamics. First, we apply conservation of momentum to determine what fraction of the initial kinetic energy goes into translational energy of the gas cloud. Second, we assume that all the remaining energy, both kinetic and chemical, is converted into internal energy of the gas cloud. Finally, we compute the dynamics of a hot expanding gas cloud using simple fluid-dynamics analysis.

Analysis

Assume an impactor of mass m_i moving at velocity v_i, kinetic energy W_i, hits a stationary target of mass m_t that releases chemical energy W_{chem} after the collision. Assume that the combination of projectile and target has no net angular momentum (head-on collision) and that the collision is totally inelastic. Assume that the projectile and target are vaporized completely due to the collision. We realize that this is not a good assumption because there is a stress gradient in the lexan projectile and the maximum stress responsible for the dissociation will be concentrated around the first half of the projectile from the impact interface. Momentum conservation implies that, after the impact, the debris cloud will have a center-of-mass translational velocity v_{cm} given by

$$v_{cm} = \frac{m_i}{m_p + m_t} v_i \qquad \textbf{(1)}$$

The associated kinetic energy, W_{cm} is

$$\begin{aligned} W_{cm} &= \frac{1}{2}(m_p+m_t)v_{cm}^2 \\ &= \frac{1}{2}(m_p+m_t)\left(\frac{m_i}{m_p+m_t}\right)^2 v_i^2 \\ &= \left(\frac{m_i}{m_p+m_t}\right)\times\frac{1}{2}m_i v_i^2 \\ &\equiv f\times W_i \end{aligned} \qquad \textbf{(2)}$$

with the remainder of the initial kinetic energy going into thermal energy of the debris cloud. Consequently, in the center-of-mass frame of reference of the debris cloud, the gas energy is

$$W_{gas} = W_{chem} + (1-f)\,W_i \qquad \textbf{(3)}$$

Numerical Evaluation

In the experiment, m_i = 28 gm, vi= 5.6 km/s *wi*= 439 kJ), and *mt* = 5.6 gm (1-f = 16.7 %). The target (comp B) consisted of 40% TNT and 60% RDX, by weight, which have explosive energies of 250 kcal/gm mole and 335 kcal/gm mole, respectively. The atomic number of TNT is 227 and of RDX is 222. Consequently, the target had 2.24 gm (9.87e-3 gm-moles) of TNT and 3.36 gm (1.51e-2 gm moles) of RDX, with explosive energies of 2.47 kcal (10.3 kJ) and 5.07 kcal (21.2 kJ), respectively. Thus *Wchem* = 31.5 kJ, and W_{gas} = 31.5 kJ + 0.167*439 kJ = 73.3 kJ. Slightly more than half the gas-cloud energy came from the kinetic energy of the projectile.

Gas Cloud Behavior

We model the gas cloud behavior with an idealized fluid-dynamics model. Zeldovich and Raizer [2] present an analysis of spherical expansion of a gas cloud based on earlier work by Stanyukovich [3]. They point out that, while the flow depends in detail on the initial conditions, the flow asymptotically approaches a self-similar solution. Some information about the initial conditions is frozen in, including the shape of the radial profile of the gas density. The gas cloud cools as it expands by doing pdV work and radiative cooling is neglected because it is much slower.

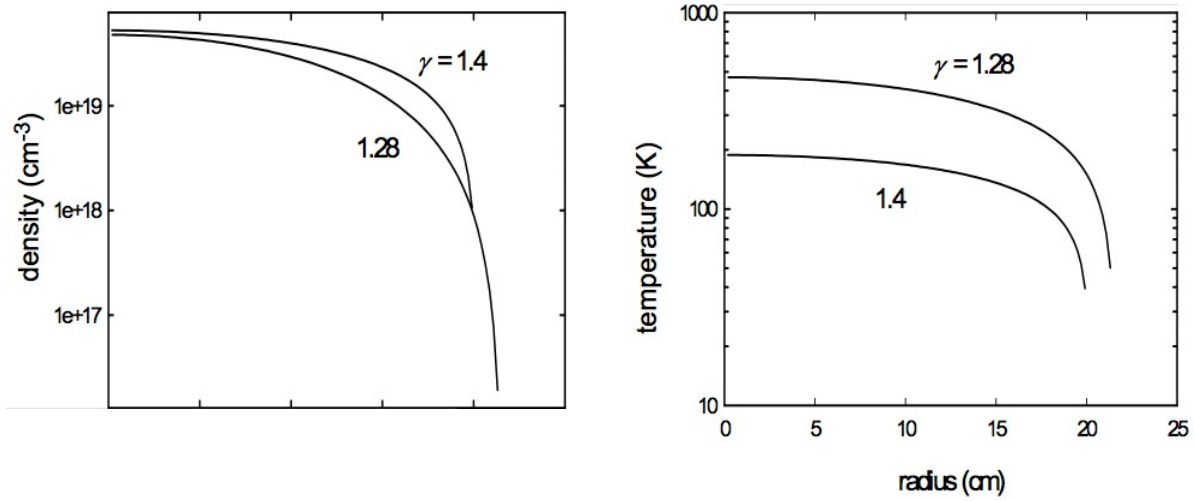

Figure 2. Computed density and temperature profiles of ideal spherical expansion of 33.6 gm of gas at 35 μs. Initial conditions: radius = 1.4 cm, temperature = 3200 K.

In the center-of-mass frame of reference, the cloud is taken to be an initially hot, uniform sphere of ideal gas that undergoes spherical expansion after the impact (t = 0). The gas has mass 33.6 gm and initial energy W_{gas} = 73.3 kJ. We take the initial radius of the gas cloud to be the radius of the target disk, or 1.4 cm. The detonation products of comp B are dominated by H_2O (40%), N_2 (34%), and CO_2 (19%), with a total of 31.4 moles (1.89e25 molecules) generated per kilogram of explosive.

The gas cloud will contain a mixture of comp B products and Lexan products. We have little information about the latter. We will boldly assume that the Lexan products are the same as the comp B products. In that case, for a total cloud mass of 33.6 gm, there are 6.35e23 molecules, and an initial thermal energy of 1.15e-19 J/molecule, or 0.72 eV/molecule.

The gas cloud consists of a mixture of diatomic molecules (N_2) and tri-atomic molecules (H_2O and CO_2) which have isentropic exponents (ratio of specific heats, γ) of 1.4 and 1.28, respectively. It is not clear how to treat such a mixture of gases. Figure 2 shows computed results at t = 35 μs when the gas cloud is 40 cm in diameter, for the two cases of pure N_2 (γ = 1.4) and pure CO_2 (γ = 1.28), both at 3200 K initial temperature. This temperature was chosen to give initial energies approximately equal to W_{gas} computed above (73.3 kJ). The value 3200 K corresponds to initial energies of 79 and 71 kJ for the N_2 and CO_2 cases, respectively. Associated with such a high initial temperature would be bright optical emission that would decay quickly. This high temperature is probably beyond the range where the ideal gas law is accurate for these species.

The computed edge expansion velocities for N_2 and CO_2 are 5.75 and 6.15 km/s, respectively. Inside the gas cloud, the gas radial velocity increases linearly with radius. These edge velocities are comparable to the projectile velocity (5.6 km/s) and to the center-of-mass velocity (4.7 km/s). This means that, in the lab frame of reference, the center of the cloud would drift downstream somewhat slower than the upstream edge of the gas cloud would move upstream. Consequently, the upstream edge would move upstream at approximately 1 km/s while the downstream edge would move downstream at approximately 10 km/s.

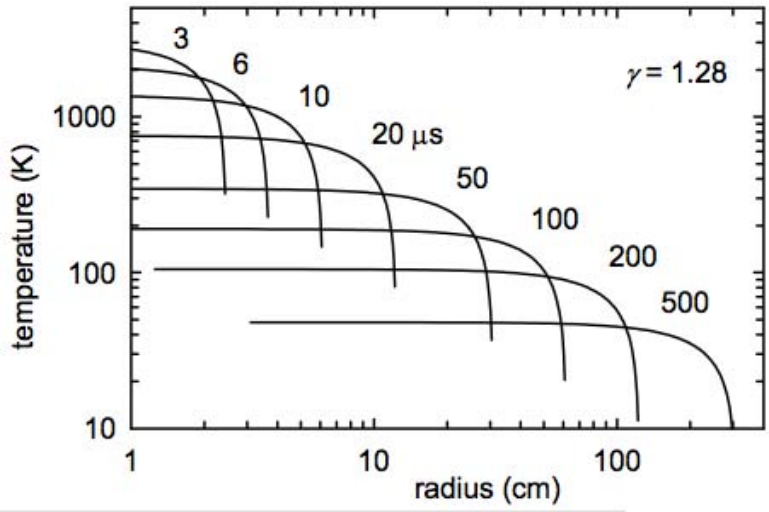

Figure 3. Temperature profiles at various times for the case γ = 1.28.

Figure 3 shows the series of radial profiles of the gas cloud temperature at various times for the CO_2 case. For the other case ($\gamma = 1.4$) the shapes are similar but the temperatures are lower, as indicated in Figure 2. Note that at late times, the gas cloud is calculated to get very cold.

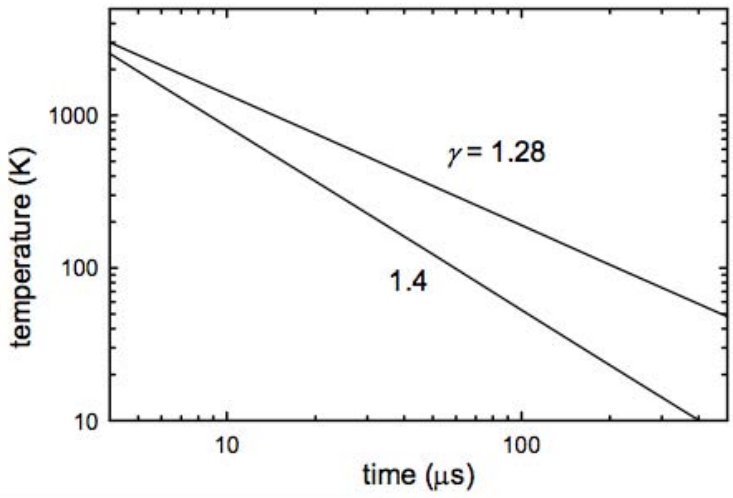

Figure 4. Temporal history of gas temperature at the center of the gas cloud.

Figure 4 shows the time history of the temperature at the center of the cloud. Initially, the gas would emit bright optical emission because of its high temperature. As the cloud expands, the emission area (surface area) increases approximately quadratically with time, but the temperature drops rapidly. The emission intensity at any particular wavelength would depend on the combination or temperature, cloud radius, and opacity at that wavelength. At late times (>> 100μs), the gas-cloud temperature is computed to fall below liquid-nitrogen temperature. Of course, gas condensation and external interactions, such as those with nearby walls and any residual background gas, would limit the actual temperature drop.

Comment

The computed behavior is for an idealized case of spherical expansion of a gas cloud. We have described the gas by the ideal gas law with constant γ, we have neglected any liquid and solid particles that might be present, and we have assumed a perfectly inelastic collision with all the excess energy going into internal energy of the gas. Consequently, the results can only be expected to provide general guidance rather than detailed, quantitative predictions. As will be shown later, the temperature estimate of the radiating debris is much higher than what the above calculation suggests.

2.2.2 Calculating THz Absorption Coefficient of Comp-B Byproducts

Overview

Modeling was performed to develop a conceptual understanding of attenuation of terahertz frequency radiation for a mixture of products in vacuum over a short path length (L = 1m.) A simple model was used to explore this question for the temperatures 70K, 100K, 278K and 1000K and pressures 1mb (millibar), 10 mb and 100 mb. (Note: some of these were actually computed early on to help define the experiment, whereas the equation of state calculations were done after the fact in an effort to understand the data better.) The results of this section are used to calculate the emission spectra of the gas in section 2.2.4.

Method

A line-by-line radiation transfer model was used in this study in conjunction with the HITRAN spectroscopic database. The radiation transfer code utilized was LBLRTM version 9.4, which is maintained by Atmospheric and Environmental Research, Inc. (AER) and is a FASCODE derivative code [http://rtweb.aer.com]. The spectroscopic database utilized was also obtained from AER version 1.0. This database is essentially the HITRAN2000 database with modifications.

Details

The desired list of compounds is listed in Table 1. Of the 16 compounds, 11 were in the LBLRTMs database. The column LNFL ID# indicates the identification number where available and x indicates the lack of that compound in the spectroscopic database. When using a user defined atmosphere profile, as was done in this simulation, the compound C_2H_4 is unavailable for inclusion.

Table 2. Subset of detonation by-products of Comp-B used for calculating THz absorption

Comp-B detonation by-products				
By-Product	*Mol/kg*	*% in Mixture*	*ppmv*	*Lnfl id#*
H_2O	12.48	39.74961053	397496.105	1
N_2	10.74	34.20759752	342075.975	22
CO2	6.089	19.39386046	193938.605	2
CO	2.078	6.618564958	66185.6496	5
NO	0.005885	0.018744107	187.441072	8
CH_4	0.002952	0.009402312	94.0231172	6
O_2	0.000677	0.002156289	21.5628897	7
CH_2O	0.00002004	0.0000638287	0.638287015	20
C_2H_6	1.133e-009	3.60868e-009	0.000036086786	27
NO_2	1.616e-012	5.14706e-012	5.14706495e-008	10

The list in Table 1 is the ideal set of information. As indicated above, only 10 of the compounds could be modeled in this simplified model. The actual concentrations used differ slightly, as well, so that the available 10 compounds accounted for 100% of the molecular species in this modeled atmosphere. The actual concentrations used in this effort are listed in Table 2.

The temperatures used in the simulation were ideally to be 50K, 100K, 278K and 1000K. However there was a problem with the partition functions below temperatures of 70K resulting in the code not functioning therefore 70K was the lowest temperature used in this work.

Figure 5 shows the results from these calculations for the gas pressure of 10 millibar at the four different temperatures. As expected the high frequency lines begin to disappear as the temperature drops due to decreasing thermal occupation of the highest levels. While the number of lines is decreasing the strength of the remaining lines is increasing. We will see later that ironically as the gas cools the emission stay relatively constant (when the gas is not optically dense).

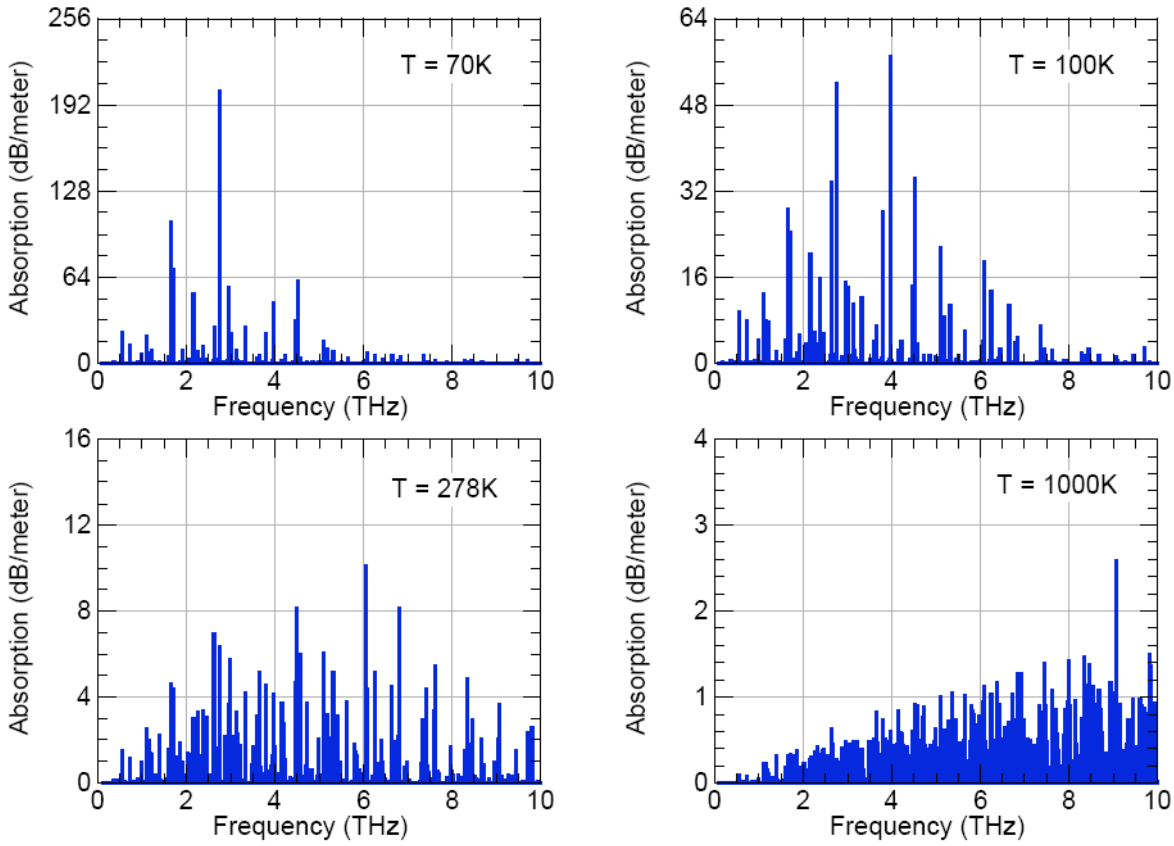

Figure 5. Spectral absorption for a gas cloud of Comp-B byproducts for a 1 meter pathlength and a gas pressure of 10 millibar. The vertical scale decreases by a factor of 4 for each temperature jump.

The effect of changing the density at fixed temperature is shown in Figure 6 . For the strong lines increasing the pressure mostly changes the linewidth of the absorption lines and has only a little affect on the peak absorption value. Around 1 THz, the linewidth observed is close to 30 MHz, 300 Mhz and 3 GHz for 1 mb, 10 mb and 100 mb respectively.

Weak lines that are seen at lower pressures, however, broaden and blend into the background absorption which also increases with pressure and hence the number of discernible lines decreases. At the higher pressures, almost all the identified peaks are H_2O and CO. Therefore low pressures will be required for high specificity gas detection.

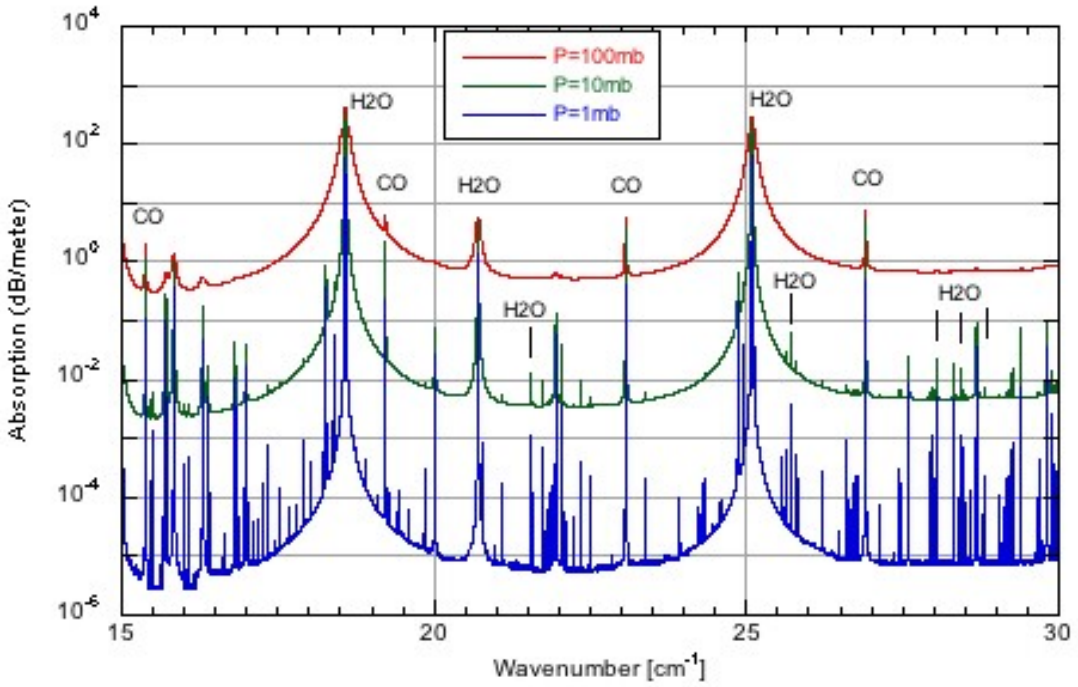

Figure 6. Spectral absorption for gas cloud of Comp-B byproducts for a 1 meter pathlength with gas pressure of 1, 10 and 100 mbar, over 15 to 30 cm^{-1}.

Since the vacuum chamber is not perfect, another set of data was generated that mimics air leaking in to an experimental vacuum chamber resulting in a background of 0.1mb with 10%, 30% and 50% relative humidity at room temperature. To accomplish this task, the US standard atmospheric model data was used with a single layer model with the chosen relative humidity forcing the overall pressure of the mixture to have a combined pressure of 0.1mb. The results were useful for calculating the background signal for the experiments.

Comments

The resolution used in this work is quite high, so that narrow absorption lines appear with little smearing with adjacent aspects of the absorption spectrum. This results in very strong, but narrow absorption lines. To compare with other experimental data, something to the effect of doing a running average or multiple channel smoothing function is required. The HWHM of the scanning function used in these simulations is 0.0003 cm^{-1} (~10 MHz).

We also did not include doppler broadening. Thus the results take into account the intrinsic linewidth and the pressure broadening of the lines, but assumes the cloud is effectively stationary. As already mentioned, around 1 THz, the linewidth observed is close to 30 MHz, 300Mhz and 3 GHz for 1 mb, 10 mb and 100 mb respectively. Given that the edge of the cloud is

expanding with respect to the center-of-mass with a velocity, u, of approximately 5 km/s, the doppler shift is given by

$$\nabla \nu = \left(1 - \sqrt{\frac{c-\nu}{c+\nu}}\right) \times \nu_{source} \approx 0.000016\,\nu_{source} \qquad \textbf{(4)}$$

or close to 16 MHz when we are looking straight through the center of the cloud. Thus doppler broadening will become important when the pressure drops below 1 mb, but given the other approximations used, the doppler shift was ignored.

2.2.3 Calculating Total Spectral Absorption

Optical Depth

The previous section discussed the calculation of the attenuation in dB / meter for various temperatures and pressures. The emission from the cloud will depend on the total absorption for the cloud column observed by the optics. The total absorption depends on the column length, density, and temperature of the cloud at the point that the detector is observing. As seen in Figure 15 we used two optical beam paths for this measurement. The first was 300 mm downstream from the impact sight and the second was 400 mm downstream. For the purposes of this calculation we assume that the optical path is straight across the chamber.

Pathlength

Taking the results from section 2.2.1, the position of the front edge of the cloud can be expressed as

$$x = (\nu_{cm} + \nu_r)\,t \qquad \textbf{(5)}$$

where v_{cm} is the velocity of the cloud center-of-mass and v_r is the cloud's radial expansion velocity (relative to the center-of-mass). We have assumed that impact occurred at t = 0. The front edge will therefore intercept the optical detection path ($x = x_d$) when t = x_d / (v_{cm} + v_r). Until the front edge of the cloud reaches 292 mm there is no signal. Since $v_r > v_{cm}$ (at least in the equation of state calculation in section 2.2.1) the back edge of the cloud will never pass the detector so we can just look at the expansion of the cloud until the experiment is over (essentially once the gas collides with the chamber walls).

Figure 7(a) shows the cloud at a moment in time after the front edge has passed the optical detection path. The total path length the optical beam path cuts through the cloud, $\mathbf{D = 2\sqrt{(v_r t)^2 - (x_d - v_{cn} t)^2}}$ is plotted as a function of time in Figure 7(b).

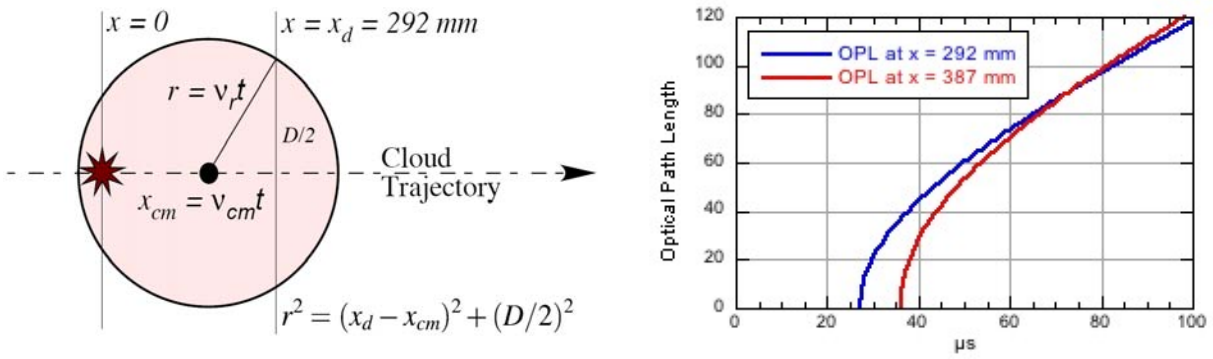

(a) Cloud Size

(b) Optical Path Length

Figure 7. (a) Cartoon of cloud some time t after impact at x = 0. The detector is at xd and sees a cloud column depth of D. (b)Assumes, vcm = 4.7 km/sec, xd = 292 mm, and vr = 6.15 km/sec corresponding to CO2 molecules.

Absorption

The total absorption, A, through the optical column of length $D(t)$, is given by the Bouguer-Lambert law $A = e^{\alpha\omega D}$ where $\alpha = \alpha(T(t),p(t))$ is the spectral absorption coefficient dependent on the temperature, T, and pressure, p, calculated in section 2.2.2, and $D(t)$ is the optical column depth just calculated. Unfortunately, α is not a linear function of p or T, thus the HiTran code should be run for every time slice for accurate results. However, this was computationally prohibitive and in the following the temperatures were rounded to the nearest value calculated (70, 100, 278 or 1000K) and α as assumed linearly dependent on the pressure with a scale factor of 1.5, using the pressure value calculated (1, 10 or 100 mT) closest to the actual pressure. The factor of 1.5 was empirically taken from the observation that the integrated absorption over a narrow region around a line appears to increase by roughly a factor of 15 as the density increased by a factor of 10.

To make the calculations easier, we also assumed that the temperature and pressure were constant inside the spherical cloud. Since we are mostly interested in H_2O, we use the temperature relation for tri-atomic molecules ($\gamma = 1.28$) from Figure 4. Mathematically, $T=9720t^{-0.848}$. The pressure is found using $pV=nRT$. The radius of the cloud is $r = v_r t$, where we used the cloud expansion velocity for CO_2 calculated in section 2.2.1, i.e. v_r = 6.15 km/sec. Assuming a cloud mass of 33 grams, and assuming all the initial materials were Comp-B which has 31.4 moles/kg, we get $n = 1.04$. To yield pressures in mbar the gas constant is, $R=.08314$. Using these values the pressure is graphed in Figure 8 . Mathematically the result is $p(t) = 8.6 \times 10^{8} t^{-3.848}$. We can see immediately that, the pressures we used to calculate the absorption coefficients will only be valid between 60 and 200 μs after the impact. Around 400 μs the pressure will reach 0.1 mbar which is roughly the ambient vacuum in the chamber.

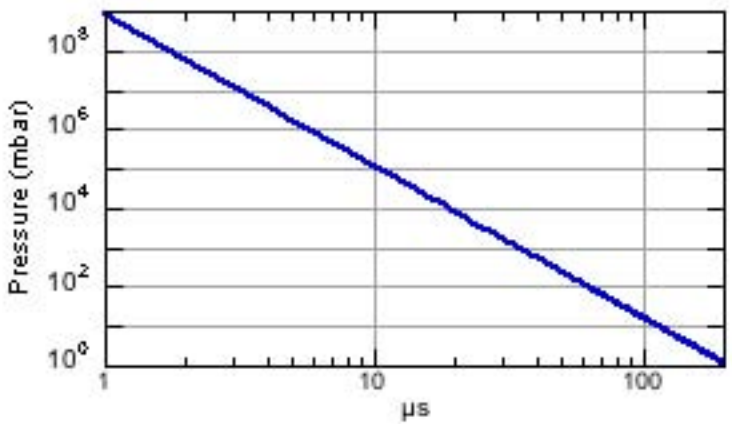

Figure 8. Pressure as a function of time assuming 33 grams of fully detonated Comp-B and $\gamma = 1.28$.

The leading edge of the gas ball crosses the optical path at 27 µs after impact, at which point the pressure is around 2.6 bar and a temperature of approximately 600 K. This pressure is significantly higher than any value we used for calculating the absorption coefficient with the HiTran database. Recall that we calculated the absorption coefficient for p = 1, 10 and 100 mbar, and for T = 70, 100, 278 and 1000K. The corresponding temperatures and pressures for these points are shown in Table 3 . From this we can see that around 64 µs, we can use α(278K, 100mb), and around 210 µs, we can use α (100K, 1 mb). For all other temperature values we interpolated as described above.

Table 3. Temperatures and pressures for the pressures and temperatures assumed when computing the absorption coefficients, the numbers in parenthesis correspond to the time after impact that these conditions occur

	1000 K		**278 K**			**100 K**	**78 K**
	30000 mb (14 µs)						
100 mb		298 K (63 µs)					
			84 mb (66 µs)				
10 mb				174 K (114 µs)			
1 mb					104 K (208 µs)		
						0.81 mb (219 µs)	
							0.16 mb (335 µs)

2.2.4 Modeling Emission

When we calculated the equation of state we assumed that the temperature dependence was related only to the cloud expansion and not due to radiative processes which are relatively small for this situation. Thus we can assume the gas is instantaneously in quasi-static equilibrium and emits like a greybody (GB). The amount of radiation reaching the detector from the cloud of temperature, T, is given by

$$\phi = L_{GB}(T)\, x A \Omega \tag{6}$$

where Ω is the solid angle of the lens seen by the detector, A is the area of the detector, and L is the radiance (W cm^{-2} sr^{-1}) given by

$$L_{GB}(T) = \int_{\kappa 1}^{\kappa 2} \epsilon_\kappa L_\kappa \, dk \tag{7}$$

where the blackbody spectral radiance

$$L_\kappa = \frac{\kappa^3 h c^2}{8\pi^4} \frac{1}{e^{\left(\frac{h c \kappa}{2\pi k T}\right)} - 1} \tag{8}$$

is multiplied by the spectral emissivity and integrated over the bandwidth (κ_1 to κ_2) that the detector can see (intrinsically or extrinsically). Note that $\kappa \equiv 2\pi/\lambda$ in this definition which is a factor of 2π larger than the values output by HiTran. Assuming Kirchoff's law holds, the effective spectral emissivity is equal to the absorptivity given by

$$e_\kappa = 1 - 10^{a_\kappa(p,T,D)/10} \tag{9}$$

We use this form since the total attenuation calculated above was in dB. For extended sources equation 6 can be re-expressed in terms of the F/# of the collection optics [4] so that

$$\phi = \frac{\pi L_{GB}}{4(F/\#)^2 + 1} A_{detector} \tag{10}$$

A couple of points are worth making in regards to the emissivity. If α = -20dB/meter the emissivity is 0.99, which is already nearly unity. This effectively means the cloud is optically dense or opaque. If we look at a much stronger line with α = -50 dB/meter, the emissivity equals 0.99999 or a change of less than 1%. Therefore the spectral emissivity may have a very different

shape than the attenuation coefficients calculated in section 2.2.2. Figure 9(a) and 9(b) are examples of the spectral emissivity. Multiplying the spectral emissivity ε_k, by the spectral radiance given in equation 8, gives the effective spectral radiance of the cloud as shown in Figure 10.

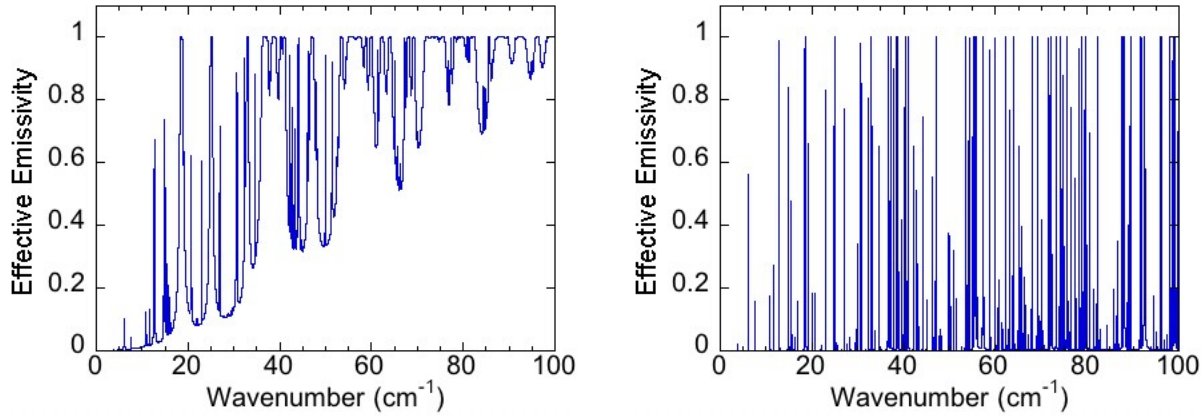

(a) Spectral emission at t=65μs (b) Spectral emission at t=210μs

Figure 9. (a) Spectral emissivity at t = 65 μs and (b) at t = 210 μs

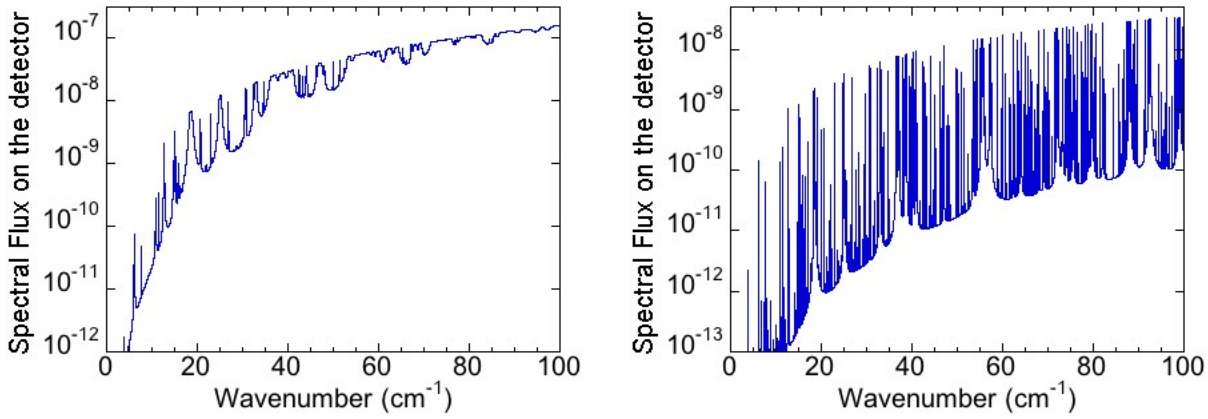

(a) Radiance at t=65μs (b) Radiance at t=210μs

Figure 10. (a) Radiance at t = 65 μs (b) Radiance at t = 210 μs

While we had originally hoped that we would be able to use a frequency selective detector sensitive enough to see individual lines being developed under a separate LDRD, the detector did not meet the specification required. Thus we used more sensitive detectors we had on hand that

were not frequency selective: a silicon bolometer and a niobium superconducting transition edge bolometer. Both of these detectors are broad spectrum detectors. Therefore instead of calculating the spectral emission we needed to calculate the radiance L_{GB} as defined in equation 7. The detectors have different low-pass cut-off filters and in some cases we used additional filters, so instead of calculating a single number we set $\kappa_1=0$ and then computed L_{GB} as a function of κ_2. The detectors have different cut-off filters and in some cases we used more, so instead of calculating a single number we set $\kappa_1=0$ and then computed L_{GB} as a function of κ_2. For the two cases of t = 65μs and t = 210 μs, the results are shown in Figure 11(a) and 11(b).

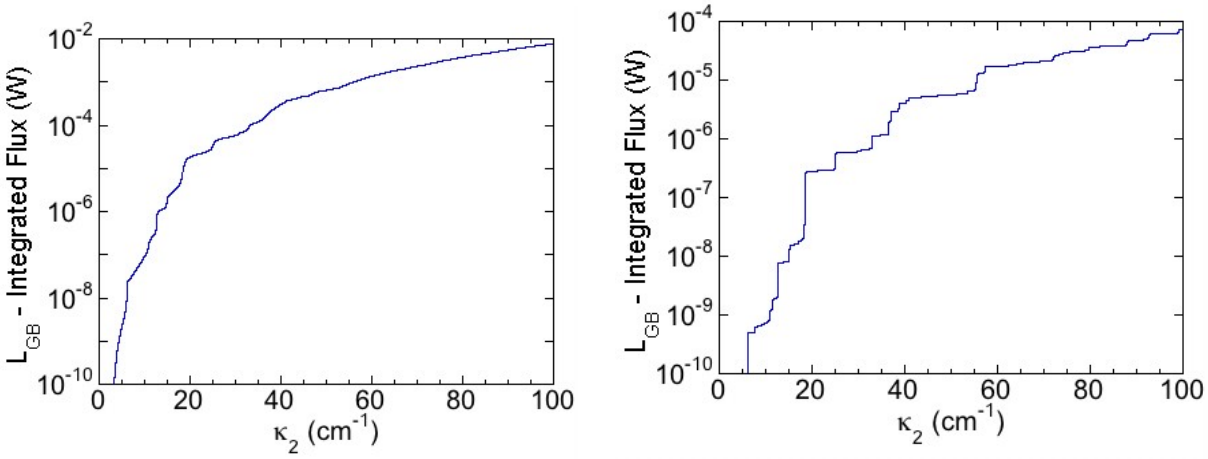

(a) Flux at t=65 μs

(b) Flux at t=210 μs

Figure 11. Flux on detector integrated over a detection bandwidth of 0 to κ_2 cm^{-1}. The flux is determined by using equation 10, assuming a detector size of 2 x 2 mm and optical F/# =2 (comparable to the Plasmon detector arrangement).

We can see from Figure 10 that if we have a detector centered on an emission line with a instrumental linewidth less than the pressure broadened linewidth, then the signal observed will decrease by around a factor of 5 between 65 and 210 microseconds. However, looking at Figure 11, the integrated signal decreases by nearly 2 orders of magnitude. The latter is a result of the substantially decreasing linewidth as the pressure drops, significantly reducing the continuum emission. This decreased linewidth also shows up as sharper jumps in the integrated flux observed at later times in Figure 11.

2.3. CTH Simulations

We have also estimated the loading and expansion behavior of Comp – B relevant to impact conditions used in this study using CTH the multidimensional hydrodynamic shock physics code. The intent of the calculation was to get a reasonable estimate on its expansion process up to approximately ten microseconds.

2.3.1 Calculation Parameters

Computational Mesh

These calculations were done using CTH in two dimensions. The problem domain was set to a rectangular area 12 cm longitudinally by 6 cm radially. A symmetry plane was used at the radial center to reduce computational requirements. Material outflow boundaries were used for the remaining boundaries.

Automatic mesh refinement was used refining interfaces and moving objects. At the highest resolution, cells would be 31.25 X 31.25 um and the problem would require 7.38 billion cells.

Material Geometry

Shot THZ-3 was simulated with a 1.43 cm radius, 2.5 cm thick lexan impactor moving at 7.682 km/s. This impacts a 1.43 cm radius, 6mm thick target assembly made up of Comp-B. The entire target assembly is surrounded by a PMMA [poly(methyl-methacrylate)] centering ring 3mm thick.

Tracers

Tracer points were inserted to track material response. Six tracers were placed (radially spaced every 2.5 mm) at each of six longitudinal locations (-2.5, -0.5, 0.5, 1.5, 3.5, 5.5 mm) with zero being defined by the impact surface. Thus, the first two locations lie in the lexan projectile, the third is in either silica phenolic or Comp-B depending on the case. The fourth and fifth locations are in Comp-B.

In addition to these 36 tracer locations, 11 additional tracers were placed in the PMMA ring. No results will be discussed from these points as it was shown that the PMMA ring does not effect the results of the simulation.

Equations of State

Lexan, silica phenolic, and PMMA were represented by Mie-Gruneisen equations of state. Comp-B is modeled using the history variable reactive burn model. The default parameters were used which incorporates a Mie-Gruneisen equation-of-state (EOS) for unreacted Comp-B and SESAME table data for the reaction products.

Material Strength

Due to the high temperatures seen upon arrival of the shock in these materials, it was determined that the materials melt almost instantly. Thus, strength (both elastic and spall) were not

included. This is equivalent to pre-melting the materials. Results of calculations run with strength included showed no difference to those without the strength models included.

Computational Resources

These calculations were run on the SNL Thunderbird Linux cluster using 32 processors. Run time is approximately 24 hours to simulate 10 us.

2.3.2 CTH Results and Discussions

A plot of the pressure, temperature, and particle velocity profiles with time is given in Figure 12. As indicated in Figure 12a – Comp-B is loaded to almost 50 GPa for approximately 2 microseconds and released very rapidly to almost zero pressure about four microseconds after impact. This loading imparts a velocity distribution to the Comp-B target. The velocity distribution (Figure 12b) of the isentropically expanding debris cloud is estimated to vary from 10 km/s to 6 km/s. The loading is accompanied by a temperature increase to ~ 0.34 eV (4000K) which drops to approximately 0.1 eV (1160K) around 10 μs. (1eV is about 11,600K.). One interesting feature of the temperature estimate is the suggestion that during the expansion process there is a temperature gradient. The free surface is at a lower temperature than in the interior of the Comp-B debris at any given time.

The results of these CTH calculations must be regarded as approximate. The reasons are multifold. It is not clear whether Comp-B has detonated at these loading pressures. Is it in an overdriven state since the shock velocity is greater than the detonation velocity? The EOS treatment for these two extreme events would yield slightly different results. Needless to say compared to an ideal gas treatment described above the temperatures are much higher. As discussed later, the experimentally determined temperature of the radiating Comp-B debris is much higher than the 0.1 eV estimates given by CTH.

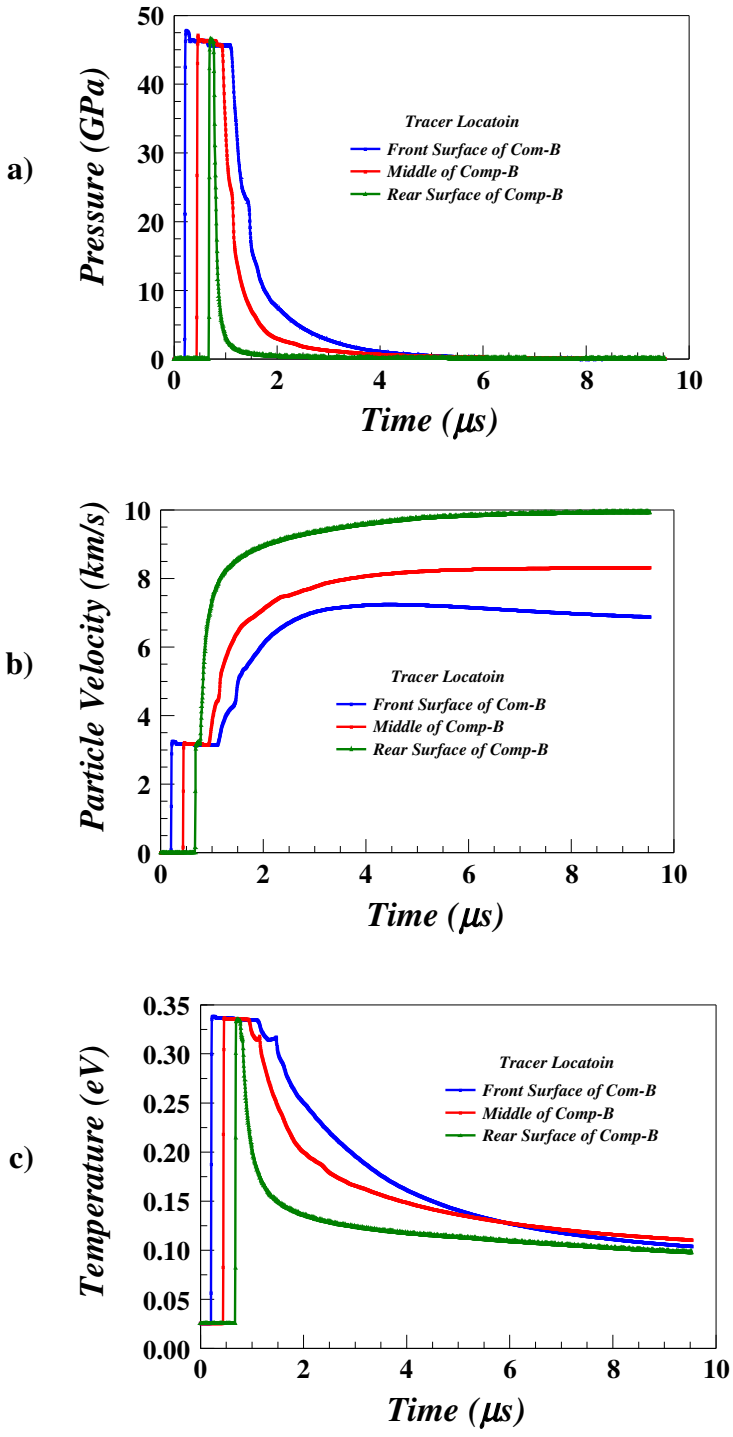

Figure 12. CTH results for a) Pressure, b) Particle Velocity, and c) Temperature.

3. EXPERIMENT SETUP

The experiments were performed at Sandia National Laboratories Shock Thermodynamic Applied Research (STAR) facility utilizing the two-stage light gas gun (TSLGG) and three stage light gas guns (3SLGG). The TSLGG is capable of attaining high impact velocities which are achieved by using the first stage of the gun to compress a light gas, such as hydrogen, to extremely high pressures and temperatures. The gas is released by the rupture of a burst diaphragm in an accelerated reservoir and accelerates a smaller projectile to a high velocity approaching 8 km/s.

The first stage of the gun is a smooth bore tube (pump tube) approximately 9 meters in length. Nearly a 7 kg polyethylene projectile (piston) is accelerated in this tube by a propellant charge in the breech and compresses hydrogen gas initially at ~ 1MPa (146 psia) to a maximum final pressure of about 1 GPa (145,000 psia). After rupture of the burst diaphragm, the compressed gas accelerates a small projectile weighing up to 30 grams (for this experimental series) in the launch tube (second stage) up to velocity of 7.7 km/s

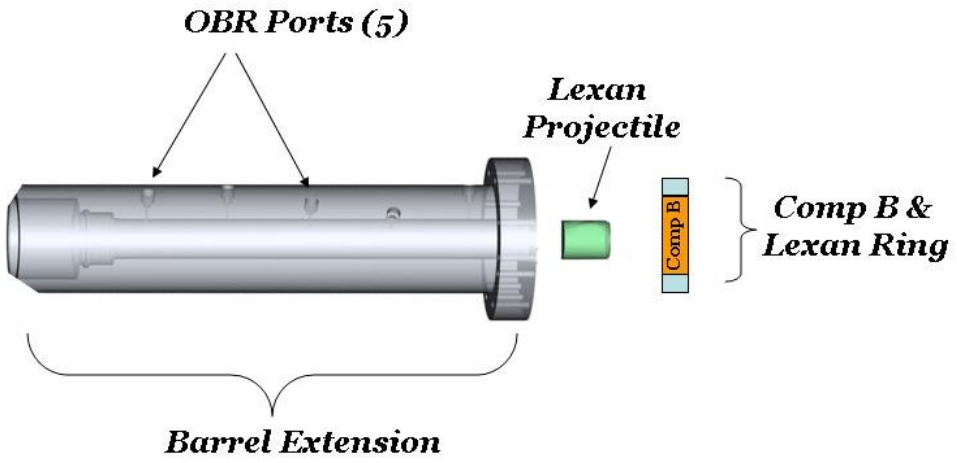

Figure 13. Impact configuration.

A unique specially designed "barrel extension" (Figure 13) is perfectly aligned to second stage launch tube (not shown) where in-bore projectile velocity can be accurately measured. Figure 13 is a conceptual schematic depicting the barrel extension, projectile and target configuration for the experiments.

Figures 14, 15, and 16 provide experimental layouts and details of the diagnostics configurations for the three types of experiments conducted in this investigation. Figure 14, is a representation

of the experimental configuration where the Terahertz, diodes, and Sandia Lightning Detector (SLD) will record the radiative properties of a debris-cloud generated from the detonation products of Comp-B. The vertical dashed lines represent the optical axis that the detectors are looking along. The detectors are on the opposite side of the port windows represented by the circles at the top.

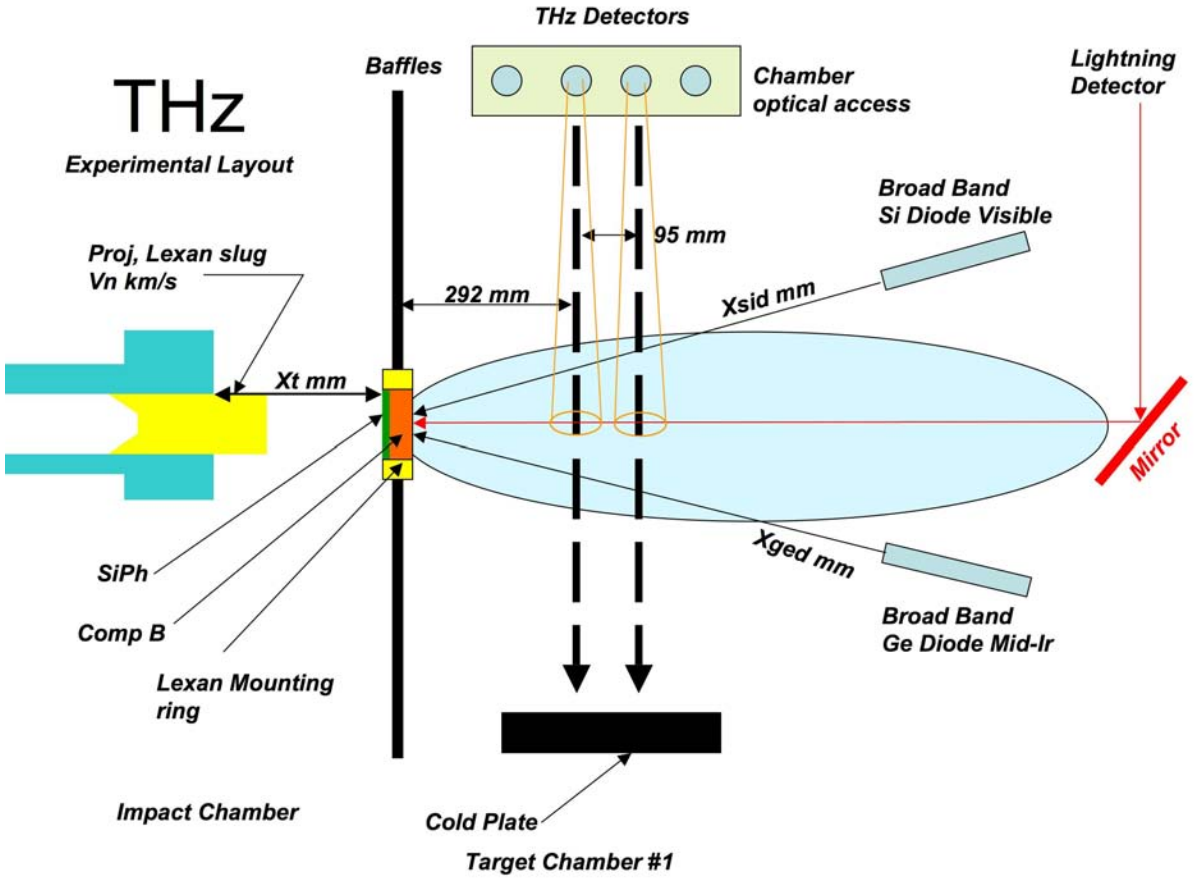

Figure 14. Experimental test configuration for Terahertz (THZ), silicon and germanium diodes, and a SLD capturing radiative properties of a debris field generated from impacting Comp - B. The Comp - B debris cloud is diagnosed for radiative emissions as it travels longitudinally and expands radially through the tank. Liquid nitrogen "cold plates" are provided for THZ diagnostics to reduce background emissions. The shaded area is an artist representation of the debris cloud.

The experimental configuration shown in Figure 15 depicts tests performed to observe Comp-B as it is impacted at various pressure states. In these tests the flyer material is changed to develop increasing impact pressure on the explosive. The flyer material used, as evident on previous experiments, does not present line emissions in the NIR. The purpose of the experiments is to provide a technique to identify line emissions of that is unique to the explosive-if they exist, and to estimate temperature of the Comp-B at various impact pressures.

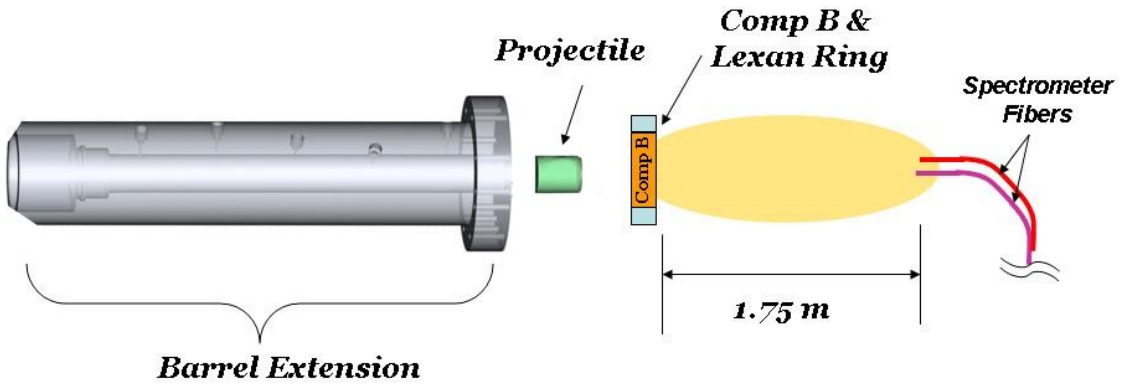

Figure 15. Experimental test and diagnostic configuration for impact experiments on Comp - B. IR spectrometers or optical multi-channel analyzers were used to observe line and radiative emissions of the expanding debris resulting from high pressure impact experiments.

The final setup, shown in Figure 16, represents the experimental configuration for the high velocity impact experiments at engagement velocities from 7 to 11 km/s using the three stage light gas gun 3SLGG. The experiments were performed to determine quantitatively the intensity of radiance from resultant impacts from a titanium flyer plate onto an aluminum target. Velocities were varied from 7 to 11 km/s and intensity at the silicon detector was obtained as a function of impact velocity and or loading pressure in the aluminum target. In addition, a four beam "silicon diode pyrometer" operating at specific wavelengths were used to estimate the temperature history of the impact surface.

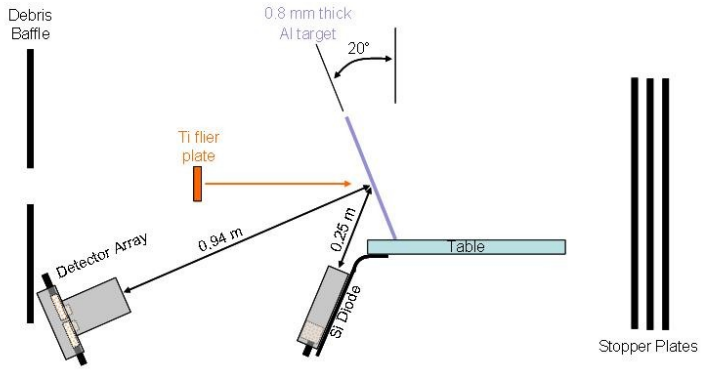

Figure 16. Experimental test configuration for silicon diode diagnostics to estimate time-dependent radiative emission and temperature histories (using silicon diode detector array).

4. THZ EXPERIMENTS

4.1. THz Introduction

The THz region may be the best frequency range in the electromagnetic spectrum for high-confidence, high-specificity material detection because many molecules, from simple diatomic chemicals to complex macromolecules have stronger and more distinctive absorption and emission resonances at THz frequencies than in either microwave or near infrared-to-visible ranges at lower temperatures as the expanding debris cools. At lower pressures, smaller molecules generally have very sharp THz signatures, providing significantly enhanced spectral resolution in contrast to infrared signatures.

An advantage of THz spectroscopy is that analysis of the rotational constants can be performed using fundamental quantum mechanics theories. With these measured rotational constants, one has an increased potential of an absolute identification of the molecule quantitatively as well as qualitatively. In most cases of interest, molecular absorption and emission cross-sections are also very large in the THz, leading to potentially excellent detection signal-to-noise levels and thus high sensitivity to small concentrations. At 1 THz the rotational energy transitions are comparable to a thermal energy of roughly 50 K, thus molecules above this temperature will emit as well as absorb at the rotational transitions. Thus for gas molecules that are at a higher temperatures than the background, the characteristic spectral features will be easily observable passively. The amount of emission of a fixed number of molecules increases strongly with temperature. These basic physical facts mean that the THz regime has enormous potential in the area of remote spectroscopy with unprecedented, unsurpassed species discrimination capability and minimized probability of error due to either missed detection or misidentification.

Multiple types of THz spectrometers exist but only a couple with speeds fast enough to capture an entire spectrum on the time scales of an experiment using the gas gun. While we hoped to use multiple THz plasmon-based detectors that we are developing, with each tuned to a separate frequency to perform a differential spectroscopy measurement, it turned out that there is not quite enough signal to use them without further improvements in sensitivity. Thus we used more broadband detectors. This limited the measurements to exploring the questions of how much THz emission is generated and how long does it last. As will be shown we demonstrated that there is significant THz emission, which lasts for long times. It is highly recommended that this investigation be continued to include more sensitive THz sensors and be conducted at later times (milliseconds) when the temperatures are anticipated to be much cooler than those observed herein. This would allow exploration of the cloud dynamics in the temporal region where the THz advantages become prominent. This would require that the experiments be conducted in a larger volume tank than those available now.

4.2. THz Detector Setup

Three different detectors were used for measuring the THz signatures. A commercial silicon (Si) bolometer [5], a commercial niobium (Nb) bolometer [5], and a new detector under development under a separate LDRD which we will refer to as a plasmon detector [6].

The Si Bolometer operating at liquid helium temperatures is very sensitive with a noise equivalent power (NEP) around 10^{-12} Watts/Hz$^{0.5}$. It exhibits a response time around 2 ms, and has a broad-band response from 150 GHz to 9 THz. For shot 2 an additional flourogold filter was placed in front of the bolometer, limiting the bandwidth to below 800 GHz. The slow response time is not fast enough to observe the temporal dynamics of the cloud, but allows the detector to see signals as small as 10 pico-Watts.

The Nb Bolometer should exhibit the same NEP as the Si bolometer. However, it has a nanosecond response time, and therefore can only see signals above 10 nW. In this case we have traded sensitivity for speed to allow us to observe the temporal dynamics of the debris field emission.

The Plasmon Detector has a NEP around 10^{-8} Watts/Hz$^{0.5}$, and has a response time around 0.1 ns. Thus the minimum detectable signal should be around 1 mW. This detector, is electronically tunable with a bandwidth around 50 GHz and for these measurements the center frequency was tuned to 800 GHz, where a strong water absorption/emission line resides. Given the low sensitivity we did not think there would be enough emission from the debris cloud to use it. However, after the large saturation of the Si bolometer on the first two tests, we decided to include it in shot number 3. Originally we had hoped to use four of these detectors, tuned to different frequencies to enable a differential spectroscopy measurement, but loss of the high mobility MBE growth capability for the year prevented completion of this effort.

To make the measurements, we decided to look through the cloud perpendicular to the clouds propagation direction (see Figure 14.). If we looked along the propagation axis of the cloud, the initial flash probably would have saturated the Si bolometer which would not have had time to recover, and we would always have been looking at hot debris particles behind the gas. In the side viewing configuration, the gas should cross the optical path first, followed by the particulates.

On the opposite side of the target chamber from the optical ports, we placed a plate large enough to cover the collection angle from the detector optics. This plate was made out of aluminum and anodized. The actual emissivity of the plate was not measured but was assumed large enough that reflections would be minimal. To decrease the blackbody radiation emitted by the plate it

was then cooled to around 77K with liquid nitrogen. This minimizes the photon background on the THz detectors.

The THz emission was viewed through two 5 mm thick quartz windows placed 292 mm and 387 mm downstream from the impact respectively. We had initially wanted to be close to the collision to get the most signal possible in order to use the plasmon detectors. Unfortunately, the modeled density is still large at this point, suggesting spectral features would be washed out if the detectors were narrowband.

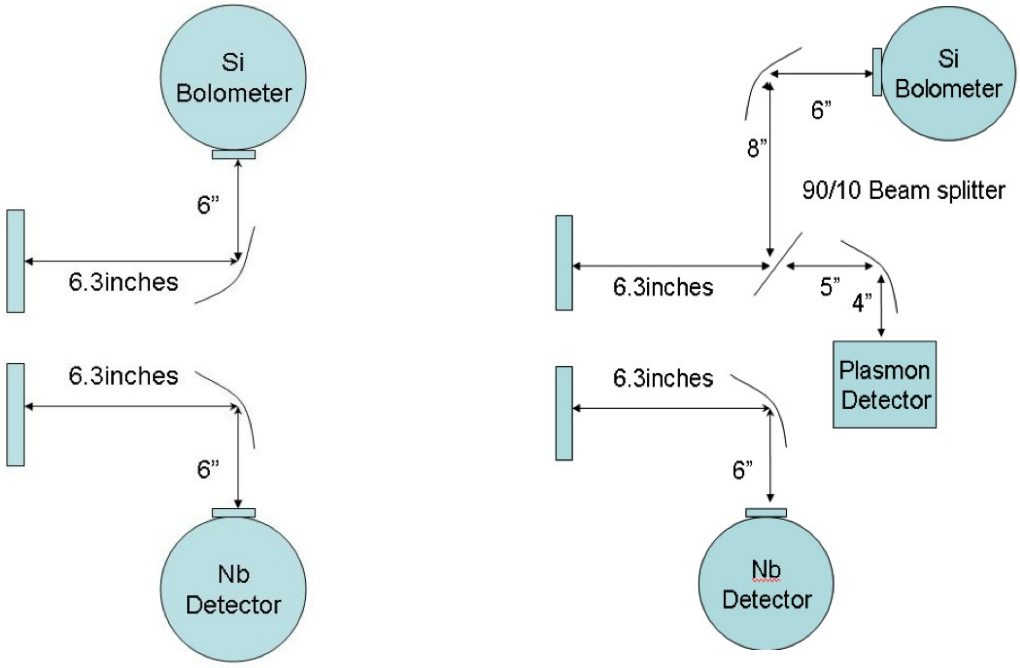

(a) Two THz Detectors Arrangement

(b) Three THz Detectors Arrangement

Figure 17. (a) Detector arrangement for shots 1 and 2 (b) Detector arrangement for shot 3 - the beamsplitter sends 90 percent to the plasmon detector. The distances between the curved mirrors and the detectors equal the focal length of the off-axis paraboloids, and the rectangles on the left represent a top view of the THz optical ports for the target chamber shown in Figure 14. The clear aperture of the ports was limited to 1.25 inches which increased the effective F/# of the optics. For shots 2 and 3 the beam path was also purged with dry nitrogen. The debris cloud in this figure travels from top to bottom.

Table 4. Experimental parameters for each shot corresponding to Figure 14.
Vn is the projectile velocity, Xt is the barrel to target distance, Xsid is the target to Si diode distance, Xged is the target to Ge diode distance and SiPh represents whether Silicon Phenolic was present on the front surface of the target.

	Vn	Xt	Xsid	Xged	SiPh
Shot 1	5.59		1105		no
Shot 2	7.0	215.9	1133		no
Shot 3	7.7	222.3	1111	1122	yes

4.3. THz Results

The outputs of each detector were connected to multiple digitizers, each set to a different sensitivity, since it was unknown how much signal there would be. The high sensitivity digitizers captured small features allowing determination of the THz onset easily, but saturated early in the pulse. The low sensitivity digitizers were able to capture the larger features without saturating. Depending on the digitizer used the data sampling occurred every 8 to 40 ns, which is significantly faster than the temporal responses observed. To clean up the signal, many of the plots below replace each point with the average of a number of points around the chosen point. The number of averages will be mentioned for each plot.

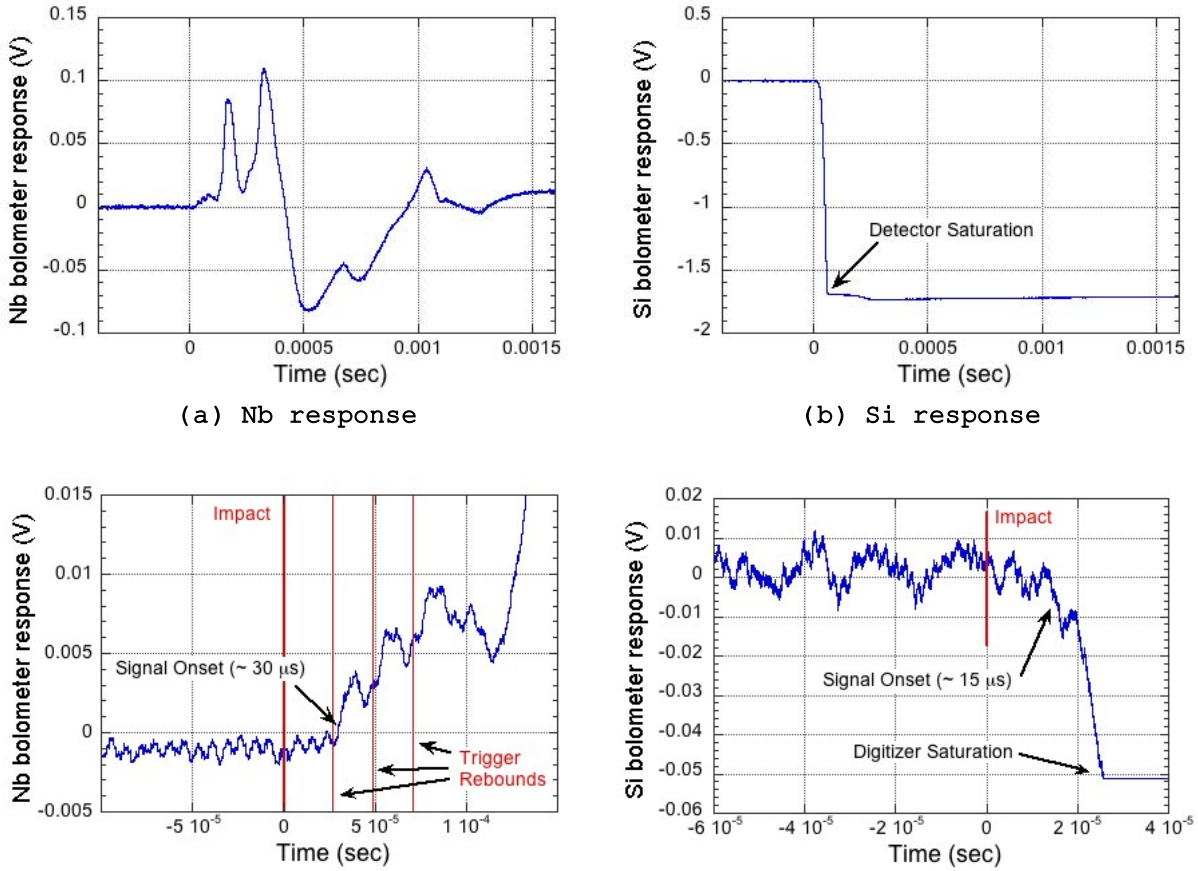

(a) Nb response

(b) Si response

(c) Nb response for the first few 100 μs after impact

(d) Si response for up to 40μs after impact

Figure 18. Results for shot 1. (a) Nb bolometer response with 500 pt (4 μs) smoothing applied (b) Si Bolometer response with 500 pt smoothing applied (c) Nb bolometer response for times close to impact and also showing initial trigger and location of random extra trigger events (d) Si bolometer response with no smoothing applied for times close to impact showing signal onset.

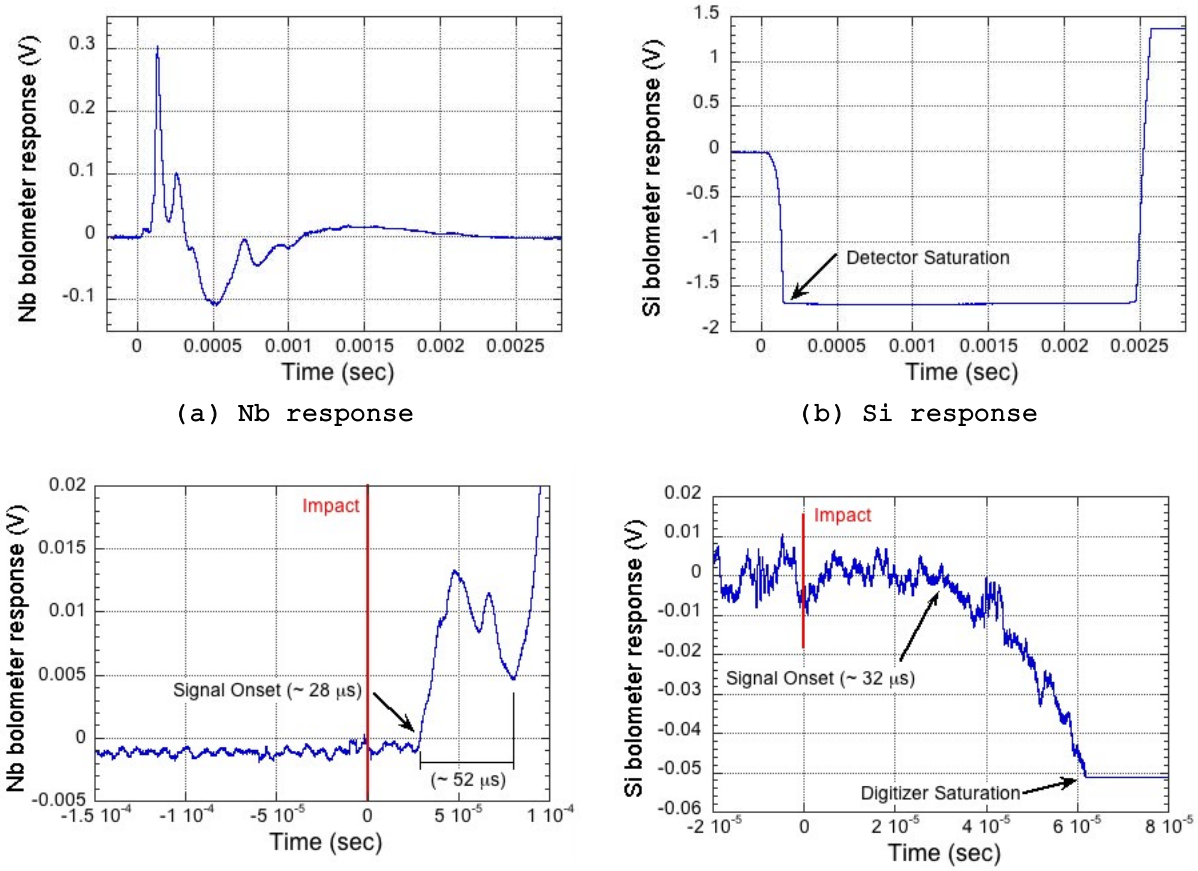

(a) Nb response

(b) Si response

(c) Nb response for the first few 100 μs after impact

(d) Si response for up to 80μs after impact

Figure 19. Results for shot 2. (a) Nb bolometer response with 500 pt (4 μs) smoothing applied (b) Si Bolometer response with 500 pt smoothing applied (c) Nb bolometer response for times close to impact. (d) Si bolometer response with no smoothing applied for times close to impact showing signal onset.

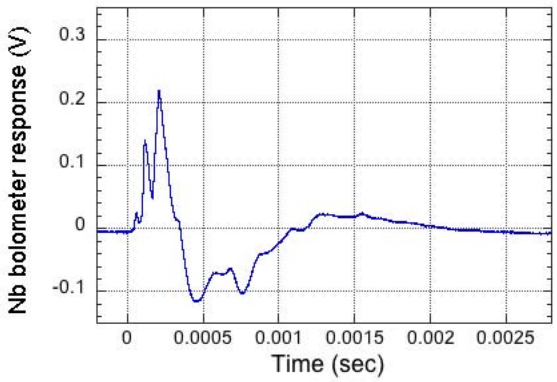

(a) Nb response

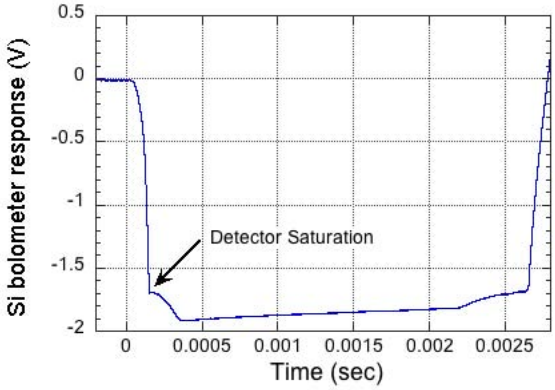

(b) Si response

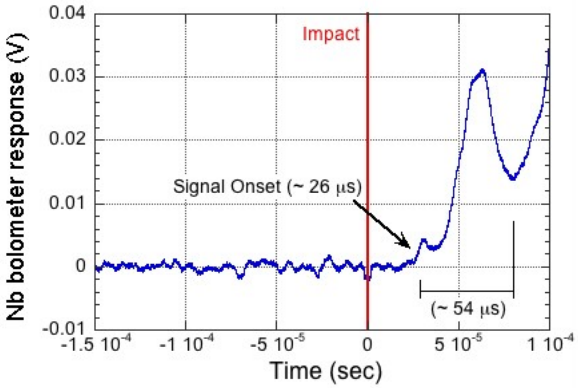

(c) Nb response for the first few 100 μs after impact

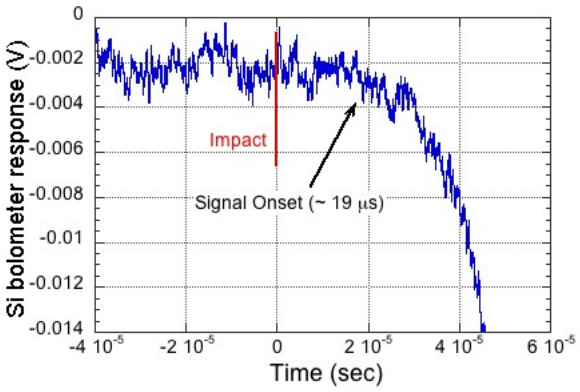

(d)Si response for up to 6μs after impact

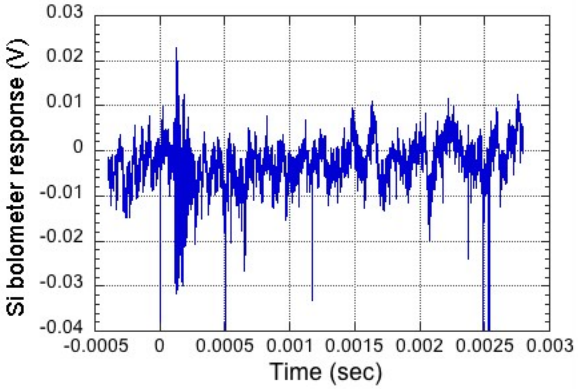

(e) PD response

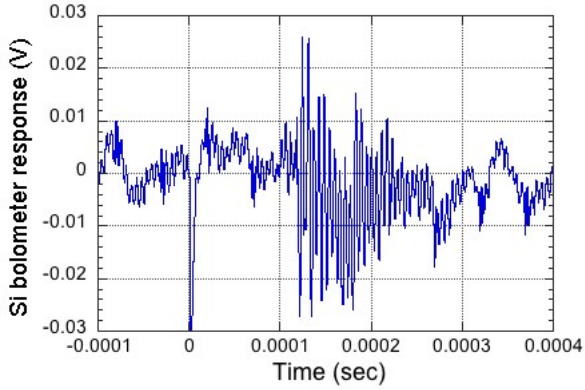

(f) PD response for the first few milliseconds after impact

Figure 20. Results for shot 3. (a) Nb bolometer response with 500 pt (4 μs) smoothing applied (b) Si Bolometer response with 500 pt smoothing applied (c) Nb bolometer response for times close to impact. (d) Si bolometer response with no smoothing applied for times close to impact. (e) Plasmon detector response (f) PD response for times close to impact.

4.4. THz Discussion

4.4.1 Shot 1

In shot 1 only the Si and Nb bolometers were used. The assumptions made in the modeling sections correlate to the projectile velocity used for this shot. The response of both detectors is shown in Figure 18.

From Figure 18(a), we can see that there is a lot going on temporally. The Si bolometer saturates almost immediately and doesn't recover on the time scale of this measurement. This suggests that there is strong THz emission from the Comp-B gas and debris cloud. From Figure 7 (based on a center of mass velocity of 4.7 km/s and an expansion velocity of 6.15 km/s) we expect the edge of the cloud to reach the optical axis of the first detector port at t = 27 μs and the second detector port t = 35 μs. The onset of the Si bolometer response (located at the first port) occurs at t=15 μs, while the Nb bolometer (at the second port) responds at t = 30 μs.. Both are faster than expected based the calculated leading edge velocity, although the silicon bolometer was much faster. This is not totally surprising because the expansion products from Comp-B may traverse much faster due to dynamic and non-equilibrium expansion behavior. Another possible explanation for the early time of arrival is unknown acceptance angle of the cone around the optical axis that the detectors can respond to. Future measurements will try to correct this. Another possible explanation for the speed relative discrepancy of the two detectors, is that due to the lower sensitivity of the Nb bolometer it takes a larger signal to observe a response and may require a longer optical path length through the cloud, delaying the effective onset.

After signal onset in the Nb bolometer there appears to be an oscillation of the response that corresponds in time to the extra trigger line excitations. While we cannot rule out the connection between the oscillation and the trigger events the overall signal between 30 and 100 μs is believed to be caused by cloud emission since it appears in latter shots where no extra trigger events occurred in this time window.

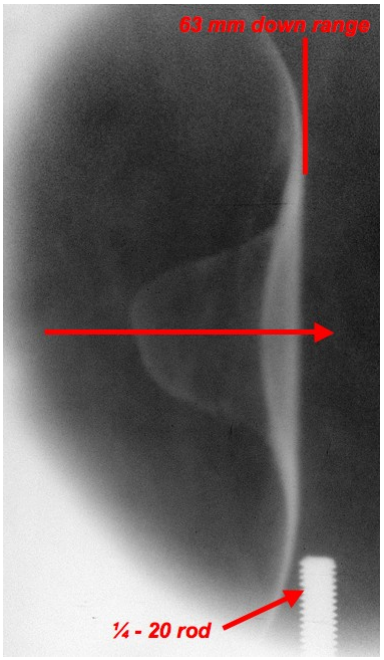

Figure 21. Radiograph of shot 1 debris cloud taken at 16.6 μs after impact.

Theoretically, the cloud should reach the chamber walls around 80 μs after impact. After this point it is unclear exactly what gives rise to the THz response since the windows will start to be coated and materials on the walls may be ejected. However the largest signals occur after this time. One possibility for the large signal rising at t = 110 μs, is that the debris cloud from the projectile may actually travel slower than the vaporized Comp-B. Figure 21 shows a radiograph of the debris cloud from shot 1 taken at 16.6 μs after impact. From its position and time, it appears that the impact interface is traveling at 3.8 km/s. This is significantly slower than the predicted impacted Comp-B gas velocity and the velocity of the gas determined by the measured bolometer signal onset. However, at 3.8 km/s, the calculated debris arrival time at the centerline of the Nb bolometer field of view is 102 μs after impact. This is close to the large measured response that starts 110μs, suggesting that the larger signals are emitted by the lexan impactor debris. Significant temporal variations continue out past the end of the measurement time of 1.6 ms, but what these could be related to is still unknown.

If the hypothesis that the initial feature between 30 and 100 μs is the Comp-B cloud and the later response is from the debris field of the lexan projectile, then we cannot place the Nb detector much further downstream to observe the gas cloud since the signal is already small. This hypothesis, however, needs to be verified.

4.4.2 Shot 2

In shot 2, again only the Si and Nb bolometers were used. In this case a flourogold filter was placed in front of the Si bolometer to limit the detection bandwidth with the hope of eliminating the saturation, and also looking at the emission intensity from the low-frequency region. The Nb bolometer had slightly different biasing conditions to re-optimize the response. The response of both detectors is shown in Figure 19.

Since the detectors had not returned to zero after 1.5 ms in shot 1, we extended the data acquisition time to 2.8 ms for this shot. The Nb bolometer has a similar response as that seen in shot one, although without the multiple oscillations at the onset. The signal onset for the Nb bolometer also appears a little sooner than it did in shot 1, which we expected given the higher projectile velocity. The Nb bolometer also appears to be settling back to zero close to 2.5 ms after impact. The silicon bolometer with a response time of a couple ms remains saturated until 2.5 ms and then rapidly changes sign which was highly unexpected. This will be discussed more below.

The more relevant information from the Si bolometer is the much later signal onset. For shot 2, the onset appears at 32 μs, which is after the Nb bolometer starts recording a THz signal even though the Si bolometer is closer to the target. If one compares the relative shape of the onset carefully in the non-saturated digitization channels one can also see that the response rises more slowly until 125 ms (see Figure 22). We currently hypothesize that the decrease in bandwidth prevented immediate saturation of the early time gas-cloud emission and thus an increasing signal as the detector continued to heat during the first 90 μs. Then the debris cloud entered the field of view at 125 ms and the rate of increase of the detector response jumps. Since the bandwidth was so limited, the detector took longer to receive the energy required to increase the response above the detector noise floor until a later time. Given that 125 microseconds is significantly delayed compared to the second peak observed by the Nb bolometer as well, another explanation could be that the optical path the detector sees may be different than in the first shot. This could be a consequence of having had to move the optics in order to open the target chamber.

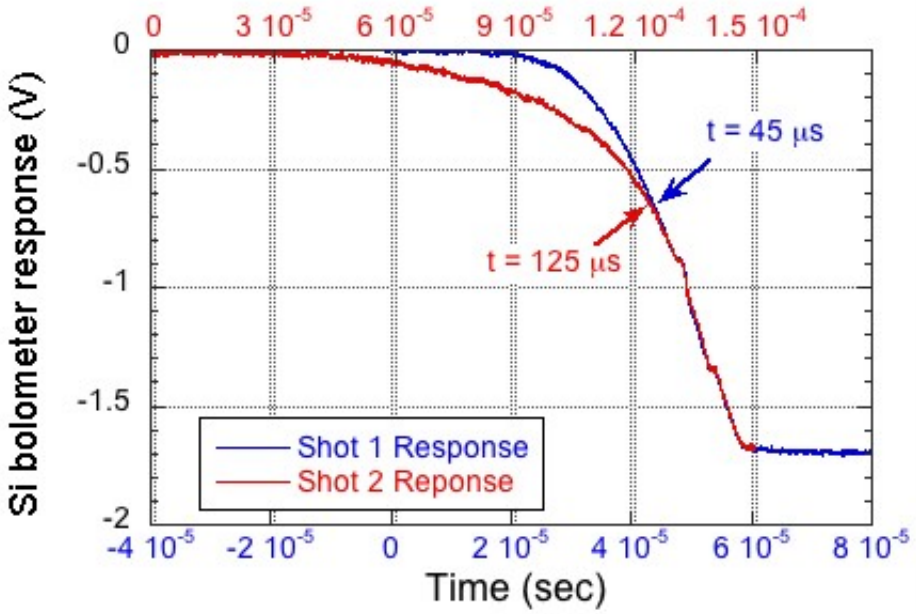

Figure 22. Relative Shape of Si Bolometer onset for shots 1 and 2. Note that the time scales are shifted and scaled so the the late time rise of the response overlaps. The relation between the time scales is t2 = (t1 - 0.000059) / 1.5

4.4.3 Shot 3

In shot 3, all three THz detectors were used. The flourogold filter was not used, but the gain of the detector amplifier was reduced by a factor of 10 and only 10% of the light through port one was directed to the bolometer. The remaining 90% was directed to the plasmon detector. The Nb bolometer again had slightly different biasing conditions to re-optimize the response. The response of all detectors is shown in Figure 20.

In Figure 20(e) the plasmon detector appears to have little response. The few large negative going spikes correspond to the excess trigger excitations, demonstrating that the electronics are sensitive to pickup and need to be shielded better. In addition there is a strong oscillation at 175 kHz throughout the measurement (including before the impact) which makes the data appears noisier than it is. Between 0.0001 and 0.0002 seconds the oscillations are significantly larger in amplitude (but they do not change in frequency). Thus it appears the detector is sensitive to the larger positive going signals observed with the Nb bolometer that we have tentatively assigned to the projectile debris field above. Unfortunately, as expected, it appears that the detector is not sensitive enough to see the early signals before 100 μs, but by comparing the size of the initial peak with the subsequent larger two peaks we can determine that if the detector sensitivity can be increased by roughly a factor of 10 it may be possible to see the early signals.

In the silicon bolometer, we again see the detector saturate, but then increase further. The increased signal after saturation on the Si bolometer actually occurs for all shots but is most

obvious in this one. This oddity of this behavior prompted us to illuminates the bolometer with a pulsed THz laser in an effort explore the bolometer response. This behavior can be recreated, by using pulses short compared to the observed rise time. A single pulse will saturate the detector around -1.7 V once the pulse energy exceeds a threshold value which we were not yet able to measure absolutely. A subsequent pulse delayed in time can then yield an further increase above the initial saturation point. A single long pulse will not cause this effect, thus it appears that there are two pulses of THz radiation to which the detector is responding. This is in agreement with the Nb bolometer which clearly observes more than one pulse of THz radiation.

Again the Nb bolometer exhibited similar behavior to all earlier shots. The signal onset is again sooner than shots one and two, further agreeing with the increased projectile velocity. The exact shape of the Nb bolometer response differs for each shot and the order of which peak is the highest changes, but the overall, pattern is the same for all three shots. It is also interesting to note that the shape of the response is very similar to the response observed with a lightning detector.

A more curious behavior in the data is that both the Nb and Si bolometers both show undershoot after the initial pulse. When excited by short laser pulses that can similarly saturate the detector response the Si bolometer just relaxes back to zero with no undershoot, suggesting it is not a result of the ac coupled amplifier. One possible explanation is that as the gas expands it continues to cool until it is colder than the cold shield. In this case there would be a net decrease in signal hitting the bolometer compared to before the impact. In this case it is possible it can see the presence of the cold cloud. This requires significantly more testing to verify and also points out that the simple modeling of the light incident on the detector needs to be modified to account for the background radiation from the cold shield as well in future measurements.

5. SPECTROMETER EXPERIMENTS

5.1. Spectrometer Introduction

Well after the initial impact the temperatures in the expanding and radiating debris are expected to be time-dependent. For most engagement conditions described in this report the temperatures of the radiating debris at impact conditions (and at high Mbar pressures) will be of the order of 1 eV (~11600 K) and will rapidly cool down to temperatures of the order of 0.3 eV (~3500 K) or less over tens of microsecond time scales. It is over this time regime that assumptions regarding black body radiation would be most acceptable. To estimate temperatures we have implemented a four band pyrometer at specific wavelengths of 340, 460, 600, and 880 nanometers, respectively. The optical time-dependent signals obtained from impact flash are recorded using silicon (Si) or indium gallium arsenide (InGaAs) diodes. In addition, the continuous spectrum measurements obtained over the wavelength regime of 300nm to 1500nm on our visible and IR spectrometers are also used to deduce the temperature of the radiating debris.

In this chapter, we describe the spectrometer set up, the procedure implemented using a well-calibrated tungsten lamp source to obtain the correction factors that is used to normalize the spectrometer response. Herein, we discuss the method to obtain the "corrected/true" spectrum using the results obtained from a near IR spectrometer for Comp-B. Because the same principle is used to correct the optical multi-channel analyzer (OMA) spectrum obtained in the visible regime, the details are omitted.

5.2. Spectrometer Setup

For the experimental series shown in Figure 15 we have focused on obtaining light emissions for the near infrared (NIR) region spanning the wavelengths from 900 to 1500-nm. The experiments consisted of measuring NIR spectrum obtained from the propagating/radiating debris resulting from the hypervelocity impact of a Comp-B target. We used a commercially available spectrometer or OMA which provided 20 μs resolution (in the NIR) with millisecond recording time. The OMA's resolution refers to integrating over the mentioned time then digitally shifting into memory. This shifting took an additional 55 μs allowing individual spectral snapshots every 75 μs.

Using standard tabulations of atomic spectral data we were able to identify strong spectral lines from all the principle materials used in the various shots. Using these results we demonstrated that the impact flash spectra were qualitatively reproducible from shot to shot with the same experimental techniques. Further, the signals were unique to the individual materials over the wide range of velocities examined, even though some velocity dependence was observed.

5.2.1 Spectrometer Calibration: Lamp Source

FEL Lamp Standard provides absolute calibration of spectral irradiance from 250 nm to 2.5 microns. This tungsten-halogen lamp standard bears the ANSI designation of FEL. It is calibrated to the 1973 NIST spectral irradiance scale. Lamp calibration is directly traceable to the National Institute of Standards and Technology (NIST) by incorporating two NIST spectral irradiance scales. This results in estimated accuracies of 2.4% at 250 nm, 1.8% at 450 nm and 1.5% over the range from 555 to 1600 nm.

A 1000 W Quartz Tungsten Halogen (QTH) calibration lamp (per FEL lamp standard) is used to provide a near blackbody spectral source with a known spectral shape for calibrating the spectrometer amplitude response.

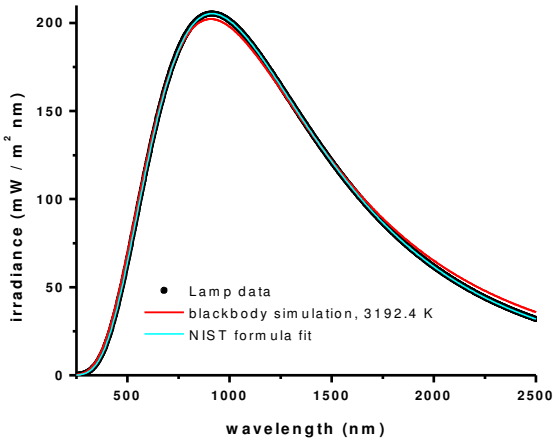

Figure 23. Spectrometer Calibration Source. Quartz tungsten halogen lamp compliant with FEL lamp standard provides near blackbody spectral source with known shape used for spectrometer calibration.

The spectrum of the lamp supplied by the manufacturer is shown in Figure 23 . The thick black line is a scatter plot of the calibration data, taken at 2 nm wavelength intervals. The red line is least-squares fit to a blackbody spectral shape with an adjustable amplitude scaling factor. The fit yielded a temperature of 3192.4 ±1.4 K. The fit is good, but not perfect, which is expected from a coiled tungsten lamp in a quartz envelope. Also shown is the waveform computed from the empirical fitting coefficients supplied by the manufacturer. This fit is essentially perfect.

With the QTH lamp source, correcting for the intensity response and incorporating the wavelength calibration, the overall spectral response of the spectrometer can be obtained. In order to determine the amplitude response of the spectrometer, the calibration of the spectrometer can be compared to the theoretical spectral shape provided by the manufacturer. This theoretical spectral shape, $\boldsymbol{B}$ is defined only as a function of wavelength, $\boldsymbol{\lambda}$ (from the

wavelength calibration-section). The spectral response amplitude correction may be made by recording the spectrum of the lamp through the spectrometer and stored in an array ***s[i]*** and generating the following amplitude correction factors for each array element:

$$Corr = \frac{B[i]}{s[i]} \quad i = 0,256 \tag{11}$$

where ***B[i]*** is the near-blackbody signal value calculated from the calibration lamp formula:

$$B(\frac{mW}{m^2 nm}) = \lambda^{-5} \times \exp(A + B/\lambda) \times (c + D/\lambda + E/\lambda^2 + F/\lambda^3 + G/\lambda^4 + H/\lambda^5) \tag{12}$$

Table 5. Manufacturers supplied constants for the blackbody spectral fit

A= 44.4180030315781
B=-4577.74614625282
C=1.00799709317016
D=-63.7795004684118
E=108234.115211209
F=-56351271.6843715
G=6972636143.49407
H=0

where the coefficients values, A-H, from equation 12, are specified by the manufacturer and shown above in Table 5. Thus, this equation can be used to find the theoretical irradiance at each of the wavelengths from the calibration lamp output.

5.2.2 Spectrometer Calibration: Wavelength

In order to obtain ***B[i],*** wavelength calibrations are performed on the spectrometer using calibrated spectral lamps with well defined spectra (this is not the QTH). For this experimental series, Krypton was the lamp of choice. From this lamp, three (3) distinct, relatively high intensity lines which correspond to the spectrometer grating setting are chosen to provide a quadratic fit. This defines spectral lines over the range of wavelengths being examined. In this manner, each sampled wavelength can be defined in terms of a quadratic expression of the index value.

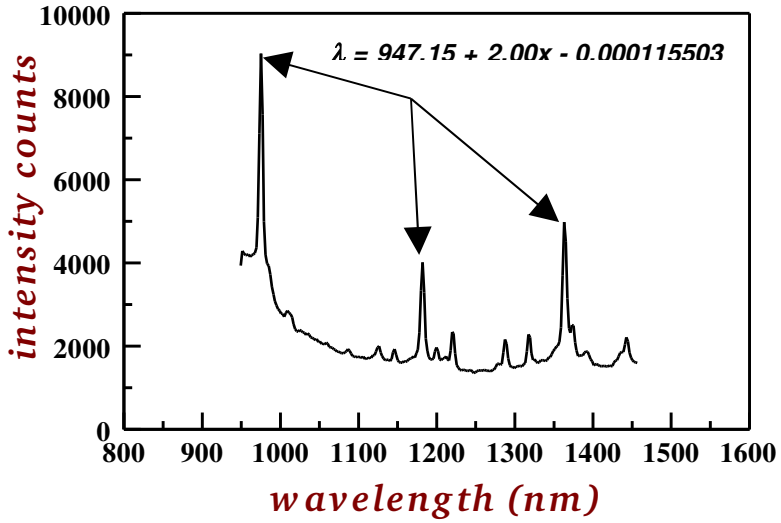

Figure 24. Wavelength calibration. Spectral lines over designated wavelength from calibration lamp. Three wavelengths define λ in terms of a quadratic expression from the x-x-axis data. The last term is omitted because it is so small.

The wavelength calibration which defines λ is determined (for this experimental series) by using the x-axis data (Figure 6). From this we obtain the formula for the wavelength:

$$\lambda = 947.15 + 2.00x \qquad \textbf{(13)}$$

Now that λ has been determined, ***B [i]*** can be obtained from the association of the wavelength with λ***[i].***

5.2.3 Spectrometer Calibration: Amplitude Correction

Once the final spectrometer spectral shape, ***B*** is defined (as a function of wavelength, λ), any measured spectrum may be converted to an effective flat spectral response by multiplying the measured spectral value with its correction term, ***corr [i],*** $i = 0{,}256$.

Equation 11 is satisfied by placing the fibers immediately in front of the QTH lamp, and recording spectra at various spectrometer settings (obtains ***s[i]***). Examples are shown in Table 6 below. Seven calibration sets were taken at the following settings:

Table 6. Spectrum recorded from the spectrometer at various gains and rates

s1: high gain 20 μs average integration time
s2: high gain 100 μs average integration time
s3: high gain 200 μs average integration time
s4: high gain 400 μs average integration time
s5: low gain 400 μs average integration time
s6: low gain 1000 μs average integration time
s7: low gain 10000 μs average integration time

The spectrum recorded is shown in Figure 25, where the lines of the 256 point arrays of data are plotted as a function of wavelength and intensity.

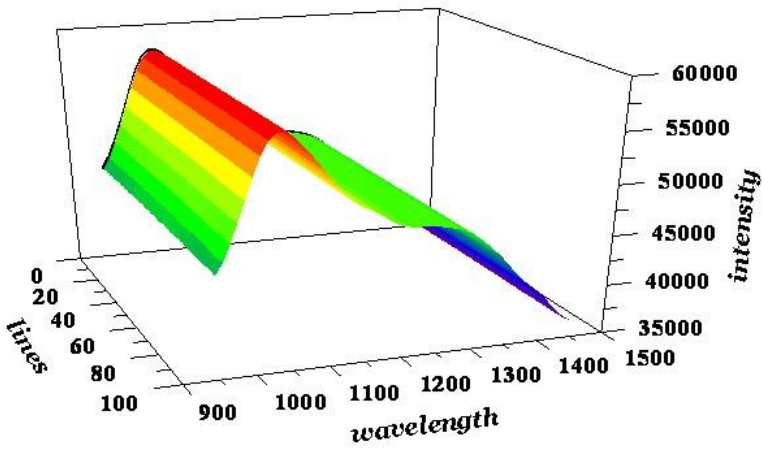

Figure 25. System calibration. Spectrum recorded from fibers looking into QTH lamp. The lines of 256 point arrays are plotted as a function of wavelength and intensity.

Figure 26 shows ratios between the spectra to check linearity response across the array. This was clearly helped by the fact that the signal did not have a huge dynamic range, partly because the response is intrinsically flatter and partly because the QTH lamp spectrum is also flatter in the wavelength region across the grating. Figure 26 shows ratios of s4/s1, s3/s1, s2/s1, s4/s2, s3/s2, and s4/s3. All ratio pairs of the three low-gain signals also gave flat responses. Combinations of high and low gain signals produced flat ratios as well.

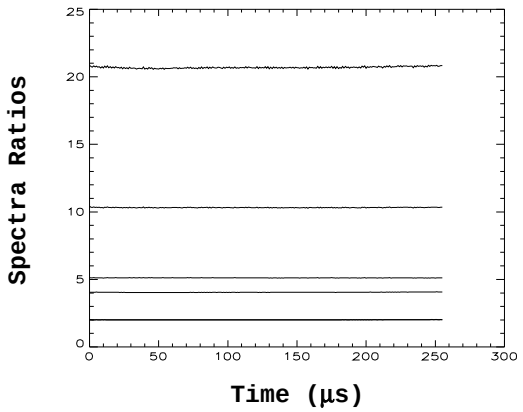

Figure 26. Spectrometer linearity check. Array linearity check indicates that the spectra taken can be used to create correction arrays which can be used on experimental data acquired at any sampling rate or gain setting for this spectrometer.

The good behavior for all the spectra taken implies that we may create correction arrays, ***corr[i],*** for each of the seven data sets. When scaled to 1 for the minimum correction, all correction arrays should look the same if things are consistent and linear. This is indeed the case, as shown in Figure 27a, which plots all seven correction arrays computed using with using equation 11 through 13 and shown as equation 14.

$$corr = \frac{B}{s\#}, \qquad corr = \frac{corr}{min(corr)} \tag{14}$$

where s# corresponds to any measured calibration spectrum. The curves (Figure 27a) all fall within the noise of the waveforms. We therefore feel justified in creating a smoother correction array by averaging all seven curves and re-scaling and shown in Figure 27b. Figure 27b shows the final smoothed correction factor array. We may apply this curve to data taken at either high or low gain or any integration time.

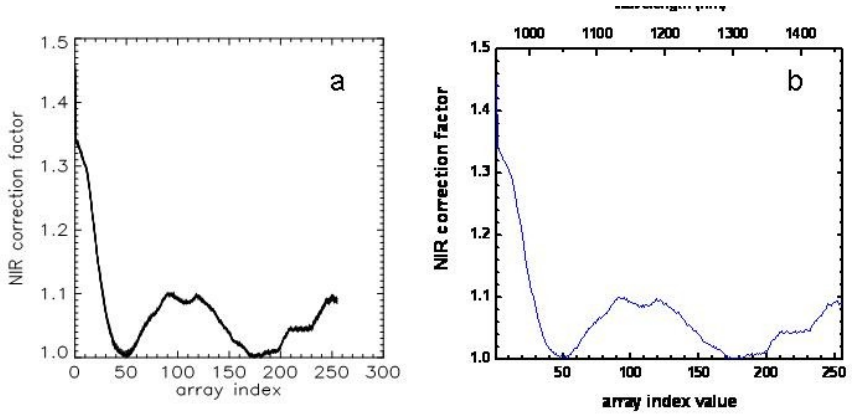

Figure 27. Final correction arrays. An overlay of (7) calibration spectra are overlayed in Figure 27a. Figure 27b shows the smoothed data of all arrays.

5.3. Spectrometer Results

We have collected time-resolved optical signatures both in the visible and near infra red regimes from a number of experiments The purpose of using this diagnostic is to provide data for determining the ability to correlate impact flash signature features to the thermodynamic details of the event that produced the flash in a realistic engagement scenario. At high velocity impacts that are commensurate and relevant to space applications, impact flash is generated due to radiative emissions. The emissions in turn will be proportional to the temperature and the temperature gradient in the radiating body. As the debris expands and cools, the mean temperature of the radiating body will be lowered. Other factors that will play a significant role is the opacity and the optical thickness of the radiating body.

Table 7. Experimental Impact Conditions

Shot Nos.	IV (km/s)	Impactor (mm)	Target (mm)[1]	Impact Pressure (GPa)
KAIF-1	6.99	25[2]	5.08	41
KAIF-2	7.11	0.5[3]	5.08	108
KAIF-3	7.04	0.5[4]	5.08	98
KAIF-4	6.99	1.06[5]	0.5/5.08[6]	460[7]
KAIF-9	5.68	25[2]	5.08	28

[1] Target will be, in all cases, nominally 5 mm thick Composition B

[2] Lexan Projectile

[3] Lexan Projectile faced with 0.5mm tantalum impactor

[4] Lexan Projectile faced with 0.5mm OFHC copper impactor

[5] Lexan projectile faced with 1.0 mm tantalum impactor

[6] 0.5mm tantalum is bonded to impact surface of Comp-B

[7] This is the impact pressure for the tantalum-tantalum interaction. Comp-B will have a lower pressure at ~100 GPa

Needless to say that it will be material dependent and each material is expected to have its unique time-dependent signature. In particular, this is the main motivating factor to develop techniques to correlate the results of the impact flash to the temperature of the radiating body. The present work explores the use of spectral and temporal content of infrared light emitted by well-defined impact generated events such as vaporized debris or explosion products to characterize the event that gave rise to the flash.

In this experimental series, for simplicity we have chosen to observe the radiance from a single material, the high explosive Comp-B. We have made measurements from five different experiments. Each experimental test was configured as shown in Figure 15. The five sets of

tests were as follows: The results obtained for the series of experiments described in Table 7 are shown in Figures 28 through 32. In all these experiments time t = 0 represent impact time at the Comp-B target.

5.3.1 KAIF-1

Figure 28 shows the spectral emission data obtained from KAIF-1 with the impact conditions described in Table 7. The data is expressed as a 3D plot displaying intensity, at various wavelengths as a function of time. At these impact conditions the Comp-B is loaded to 41 GPa.

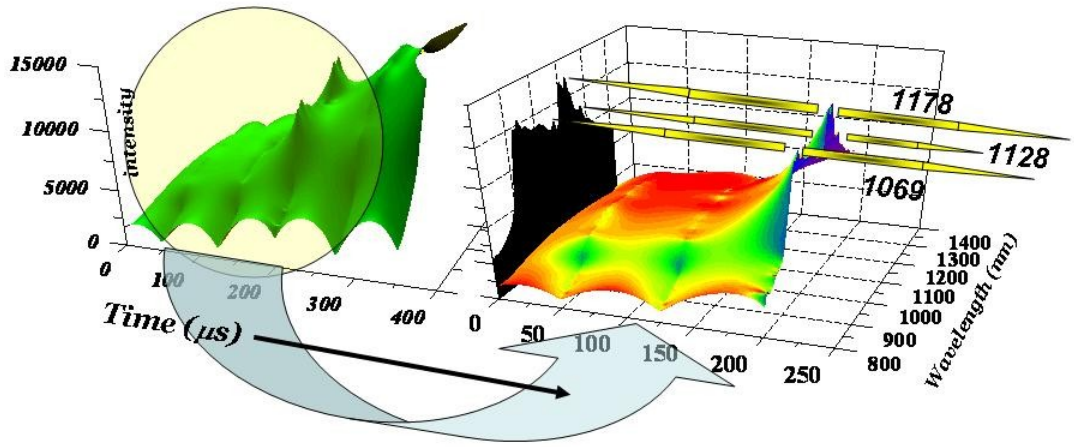

Figure 28. KAIF-1: Time dependent optical emission record in the infrared regime (800 to 1500nm) of Comp B shocked initially to approximately 41 GPa. The surface plot depicted on the left provides an overall recording of the experiment. The plot on the right is an expanded view of the area which is used to estimate temperatures. The black portion on the grid wall is a shadow portrayed on the "wall" so line emissions are easily visible. In addition, as with all of the experiments with composition B, (3) distinct emission lines at 1069, 1128 and 1178 nm are evident.

The mechanism of debris formation as the material expands after it is compressed is not clear. At these impact pressures the shock traverses faster than the detonation wave. It is not known if the material detonates or if the material is in an overdriven state. Nevertheless, upon expansion the spectral emission signatures always consists of three distinct emission lines at 1069, 1128, and 1178 nm which represent carbon, oxygen, and carbon, respectively. These elements can be directly tied to comp-B. Even though additional lines are indeed evident; these wavelengths are always exhibited when comp-B is present in the experiment. The overall continuum spectra that the emission lines are superposed on appears low in intensity providing an unambiguous identification of the emission lines. The late time spectra evolve to a nearly continuum profile which is ideal for determining temperature. The time-dependent evolution of the spectral emission can be used to determine the time-dependent temperature states of the evolving debris

cloud – assuming a black body distribution. This has the potential of explaining the thermodynamic states as the debris cloud expands to approximately 100 times its initial dimensions.

5.3.2 KAIF-2

We performed this experiment to deliberately overdrive the Comp-B to observe and differences from the previous experiment at the lower pressure state. In this experiment Comp-B is expanding from a shocked state of over 100 GPa. (The tantalum impactor is also at a 100 GPa stress loading.) As expected the continuum spectral intensity representing black body radiation is increased. This is indicated in Figure 29 which also shows that the intensity of spectral emission lines at 1069, 1178 and 1128 are increased as well.

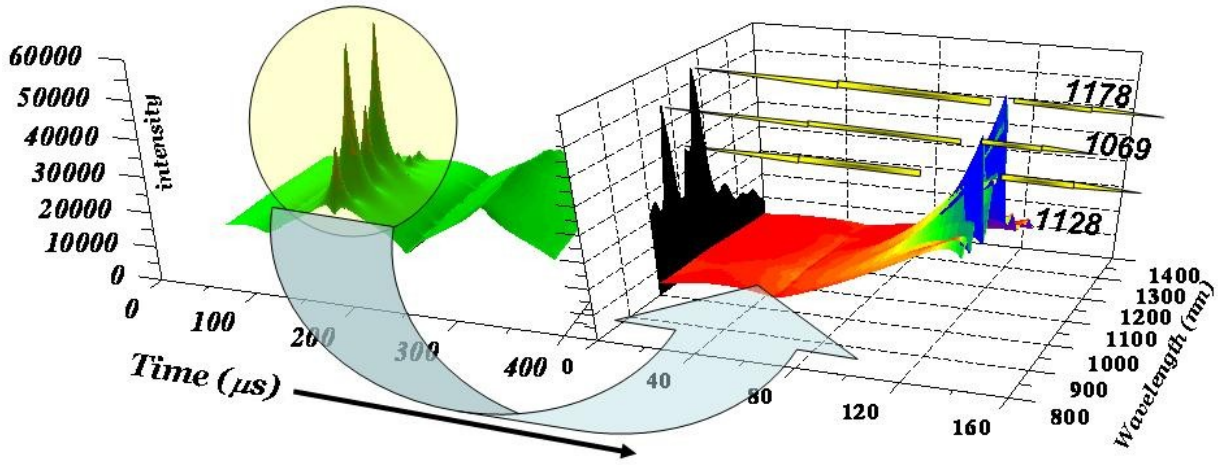

Figure 29. KAIF-2: Time dependent optical emission record in the infrared regime (800 to 1500nm) of Comp B shocked initially to approximately 108 GPa. Same emissions lines are visible on the grid portrayed by the shadow.

5.3.3 KAIF-3

Figure 30 was a test performed at an impact pressure lower than KAIF-2 yet higher than KAIF-1. A copper impactor would shock Comp–B to stresses below 100 GPa. The time-dependent spectrum indicates that the black body continuum continues to rise in intensity as the debris propagates. What is different is that the distinct emission lines at 1069, 1128 and 1178 nm seem less pronounced but still observable. It is speculated that the presence of copper impactor is contributing to the emission spectra. Additional investigation might prove interesting to determine how the emission form copper is influencing the Comp–B emission spectra.

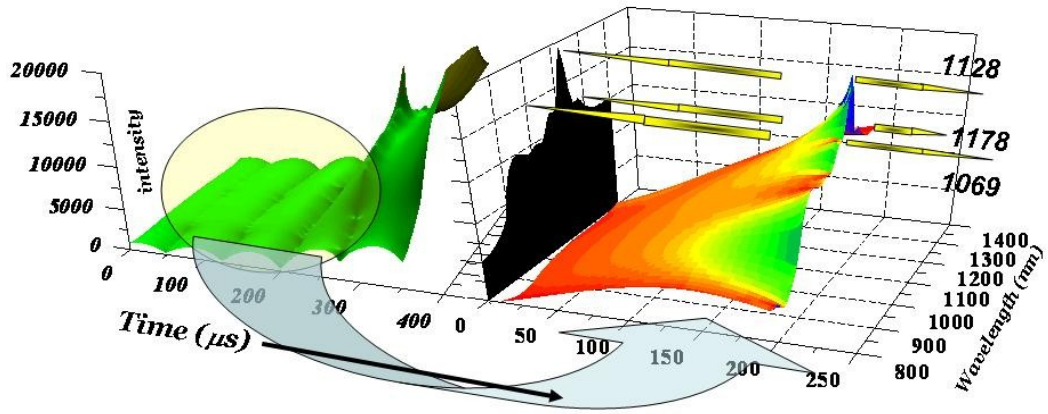

Figure 30. KAIF-3: Time dependent optical emission record in the infrared regime (800 to 1500nm) of Comp B shocked initially to approximately 98 GPa.

5.3.4 KAIF-4

KAIF-4 shown in Figure 31 was the highest impact pressure experiment. The impact stress in tantalum impactor and target is around 460 GPa. However, the pressure in Comp–B target is expected to be similar to the experiment in KAIF-2. In this experiment if the Comp-B debris is not opaque, then the spectral emission from the tantalum buffer is expected to be contributing as well. The typical emission lines at 1069, 1128, and 1178 nm are again more prominent than what was seen when copper was the flyer. It is however similar in magnitude to the results indicated for experiment KAIF-2 in Figure 29. The intensity of the black body radiation emission described as the continuum is, as expected, higher than the previous experiments. This may be a result of observing the emission spectra from tantalum expanding from 460 GPa. It is still interesting to note that no distinct spectral emission lines from tantalum are observed.

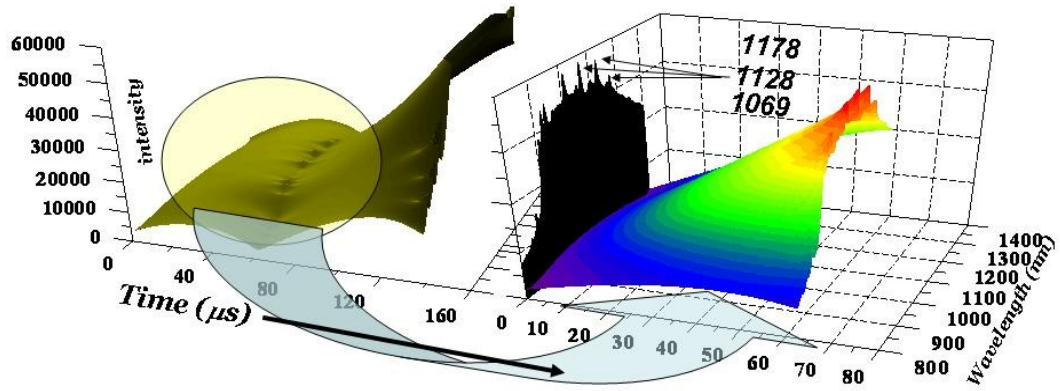

Figure 31. KAIF-4: Time dependent optical emission record in the infrared regime (800 to 1500nm) of Comp-B shocked initially to approximately ~100 GPa.

5.3.5 KAIF-9

The impact conditions for this experiment are nearly identical to those used in experiment THZ-1. Impact conditions were chosen so that the Comp-B is shocked to pressures where it is expected to detonate and not be overdriven as in the above experiments. Figure 32 illustrates that at even at lower pressures close to the detonation pressure, the spectral emission lines at 1069, 1128, and 1178 nm do exist but are very low in intensity. The black body radiation represented by the continuum emission spectrum as a function of time and wave length is also at low intensity, but appears to be increasing in intensity with time. It is possible that the lower intensity of the distinct emission lines and the spectrum is a result of lower temperatures since Comp-B was loaded only to 28 GPa. It is, however, surprising that the same characteristics of the emission spectroscopy signatures is observed over the entire stress range. This strongly suggests that either the detonation products or the dissociation products have the same constituents.

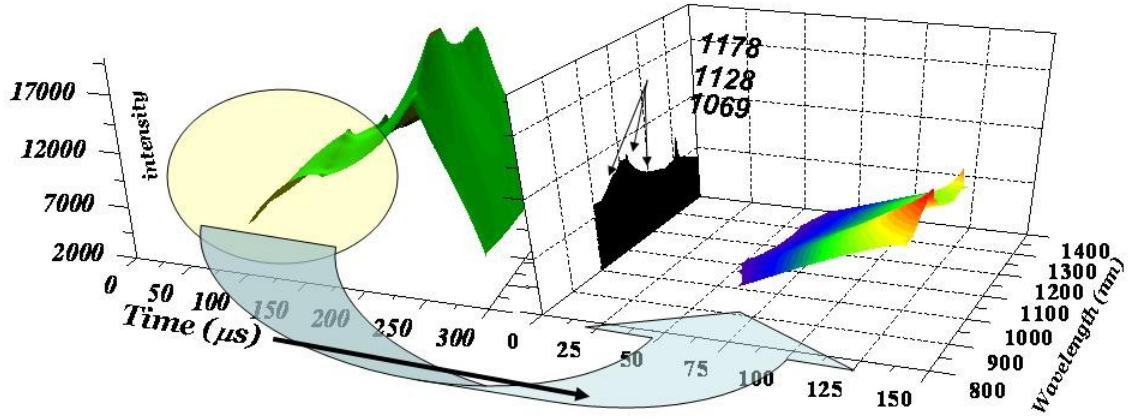

Figure 32. KAIF-9: Time dependent optical emission record in the infrared regime (800 to 1500nm) of Comp B shocked initially to approximately 28 GPa.

To summarize, we have measured time-resolved optical signatures both in the visible and near infra red regimes from a number of experiments. In this report only the infrared emission spectra is documented. The purpose of using this diagnostic is to provide data for determining the ability to correlate impact flash signature features to the thermodynamic details of the event that produced the flash in a realistic engagement scenario.

At high velocity impacts reported in this investigation, impact flash is generated due to radiative emissions. The emissions in turn will be proportional to the temperature and the temperature gradient in the radiating body. This is evidenced in this study where Comp–B is shocked from 28 GPa to over 100 GPa. The increased temperature of the expanding/radiating debris is evidenced by the increased intensity observed in the emission spectrum. The emission lines at 1069, 1128

and 1178 nm are always detected. The intensity of the emission lines are also increased when Comp–B is shocked to higher pressures (and hence higher temperatures). This is also anticipated because the intensity of the emission lines is proportional to the population density of the ionized state – which is expected to increase with increasing temperature.

As the debris expands and cools, the mean temperature of the radiating body will be lowered. Other factors that will play a significant role is the opacity and the optical thickness of the radiating body. Needless to say that it will be material dependent, and each material is expected to have its unique time-dependent signature. This is also evidenced by the presence of copper or tantalum in some experiments and appears to perturb the emission spectra of Comp-B. In particular, this is the main motivating factor to develop techniques to correlate the results of the impact flash to the temperature of the radiating body. In the next section we describe the results obtained from experiment KAIF-9 in which Comp-B was initially shocked to around 28 GPa.

5.4. Extracting Temperature from a Spectrum

In this section we illustrate how one can extract a temperature from a spectrum of a hot source. This will also serve to illustrate the errors that are inherent in this kind of extraction. We should be able to take any one of the spectra used in the calibration and treat it as if it were data from a hot source with an unknown temperature. The temperature fit should come close to the 3192.4 K blackbody temperature of the FEL lamp. We do not expect an exact match to the 3192.4K value because our FEL source is not a perfect blackbody. The fitted value will depend on the wavelength range chosen and on errors in the spectral correction process.

5.4.1 Theory of temperature fitting

We assume that we have captured the spectrum of a blackbody with gray emissivity over the spectral range of interest. The spectral shape function is given by

$$sig = \frac{s}{\lambda^5 (e^{c_2/\lambda T} - 1)} \tag{15}$$

where the second radiation constant is given by $c_2 = 1.438769 \times 10^7$ nm · K. The factor, *s*, is a scaling value that matches the blackbody shape to the observed signal. After recording the spectrum and correcting for spectrometer response, we may fit the corrected data to the function above using a non-linear least-squares routine with two adjustable parameters, *s* and *T*.

The fastest fitting routines need derivatives of the function with respect to each parameter. We have

$$\frac{\delta sig}{\delta s} = \frac{sig}{s}$$
$$\frac{\delta sig}{\delta T} = \frac{c_2}{\lambda T^2}\frac{sig\, e^{c_2/\lambda T}}{e^{c_2/\lambda T}-1} \qquad \textbf{(16)}$$

The non-linear routines also need some starting guess to begin the refinement. A simple way to get an estimate is to use the Wien's law approximation for the above function

$$sig \simeq \frac{s e^{-c_2/\lambda T}}{\lambda^5} \qquad \textbf{(17)}$$

Estimates for *s* and *T* may be made by choosing two distinct signal values, sig_1 and sig_2 at two distinct wavelength values, λ_1 and λ_2. The estimates are then given by

$$T \simeq \frac{c_2(1/\lambda_2 - 1/\lambda_1)}{\ln(sig_1/sig_2) + \ln(\lambda_1^5/\lambda_2^5)}$$
$$s \simeq sig_1 \lambda_1^5 e^{c_2/\lambda_1 T} \qquad \textbf{(18)}$$

The above formulas are used in a Levenberg-Marquardt non-linear least-squares routine to fit the spectrum to an *s* and a *T*.

We used the data from one of the NIR calibration spectra as a test of the method mentioned above. Estimates for the scaling factor and temperature were then made using the above formulas (equations 16 through 18).

The estimate is quite close to the actual value without having to do any fancy fitting. This is only because the data is not very noisy. The estimates were then placed in a parameter array and were run to extract optimized values. The temperature fit of 3224.47 is reasonably close to the overall blackbody fit value 3192.4. We conclude that the temperature fit of the corrected experimental spectrum is working as well as can be expected.

5.4.2 Estimating temperature from experimental data

KAIF-9, Figure 32, was used to estimate temperature. Figure 33 shows the output after all the calibration and fitting has been performed. As a first version of our analysis, the results show that we are *not* obtaining unreasonable results. The fitting routine indicated that the estimate was approximately 3845 K.

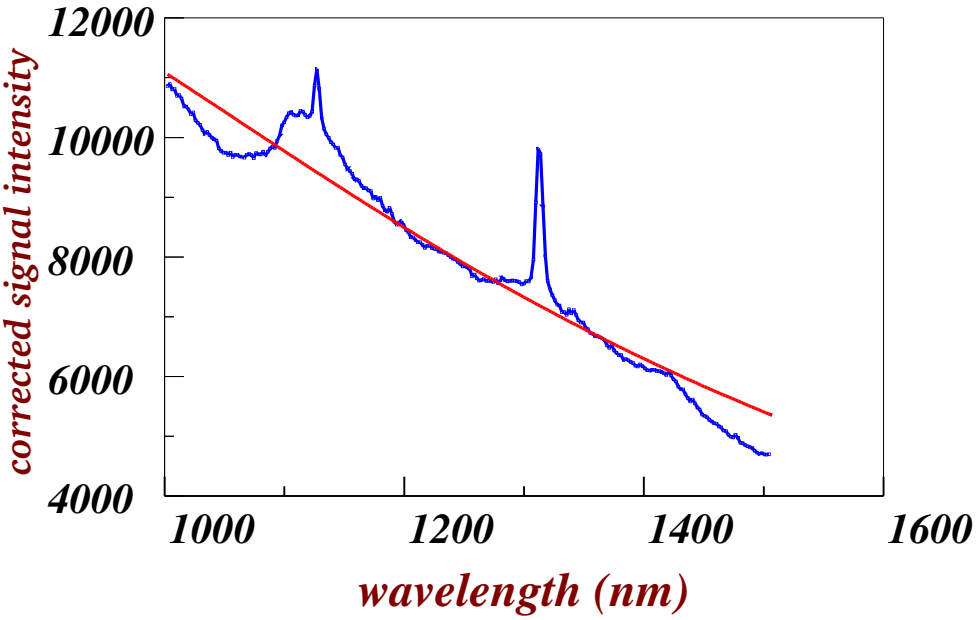

Figure 33. KAIF-9: Temperature estimate. The red line fitted through the blue data trace estimates temperature of 3845 K.

6. DIODE EXPERIMENTS

6.1. Diode Introduction

Experiments were conducted to determine the time-dependent characteristic of the optical signals that are emitted. The optical signals were monitored with several high-speed silicon, InGaAs, and Germanium photodiode detectors. The diodes observe the event either as fully exposed (no filtering) or spectrally isolated with 10 nm band pass interference filters. These diode setups were to 1), obtain intensity versus time (or velocity) from the initial impact or *prompt-flash* 2), to observe the radiating debris from the rear surface of a target after impact (including the time of shock through material until shock breakout), and 3), to determine whether a temperature can be extracted from the optical waveforms respectively. The fully exposed diodes will be referred to as prompt-flash and radiating debris diodes while the diodes containing the band pass filters will be the temperature array diodes.

6.2. Diode Setup

6.2.1 Impact Flash Photo Diode Specifications and Recording Technique

Commercial photo diode detectors were used to monitor characteristics of the resultant experimental impact flash over the visible and near-infrared (NIR) electromagnetic spectrum. Table 8 provides the specifications of the diodes used for all experimental configurations described in section 3. Signals are measured by determining the voltage across a user-supplied load resistor. 12 V batteries are used, giving a 0 to 10 V signal range for a given load resistor. 1 V into 1 MΩ represents a 1 microamp photocurrent, while 1 V into 50 Ω represents a 20 mA photocurrent. The ThorLabs data sheets indicate that the linearity limit for the silicon detector is 1 mA current or 2 mW power. This gives an upper limit of 50 mV into a 50 Ω load for the fastest linear response. The DET series detector is a reversed-biased PIN photo diode with internal battery, on/off switch, and BNC output connection in a small single package. The output is the direct photocurrent of the photo diode anode and is a function of the incident light power, diode spectral response, and wavelength. The output signal was transmitted to digitizing oscilloscopes through a 50 power divider (which splits the signal into two equal components, at exactly half the original amplitude, but maintaining frequency characteristics) and digitally recorded at two voltage sensitivities at a rate of 100 – 500 million samples per second with 50 recorder input impedance.

Table 8. Thorlabs Photo diode detector specifications

Model No.	Diode Type	Active Area A_{diode} (cm^2)	Wavlength Range λ (nm)	Detector Bandwidth (MHz)	Spectral Response Constant R(λ) (nm:Amps/Watt)
DET10A	Si	0.008	200 - 1100	350	191
DET10C	InGaAs	0.008	700 - 1800	50	683
DET50B	Ge	0.196	800 - 1800	1.6	523

For the prompt flash and radiating debris systems (RDS) these photo diodes were contained within a protective package of aluminum, and/or lexan, with the active area of the photo diode looking through a fused silica window to protect the detector from late time debris impact. The prompt flash diodes and RDS were viewing the event through a Ø 41 mm by 178 mm long steel tube. This collimated the photo diodes view onto the area of interest, effectively shielding the active area from extraneous light sources not on axis between the target and the photo diode active area. The prompt flash diode DET10A, is shown configured in Figure 16, while both DET10A and DET50B are used in the RDS configuration shown in Figure 14.

The temperature array shown in Figure 16 is also contained in a protective package of aluminum. However, as depicted in Figure 39, four diodes are in the one enclosure. The viewing tube is significantly larger in diameter and is looking directly at the impact. Each diode is covered/protected by a 10 nm band pass filter 340, 460, 600 nm for the visible silicon diodes (DET10A) and 880 nm for the NIR InGaAs diode (DET10C). In theory the narrow band filters at the various wavelengths can map out a blackbody curve providing an average temperature from an impact event.

6.2.2 Diode Calibrations

Prompt Flash and Radiating Debris Systems Diode Calibration

The manufacturer of the diodes provides typical spectral curves (Figure 34) of responsivity in amps/watt versus wavelength range (nm) [7]. The spectral curves were integrated over the detector wavelength to obtain a spectral response constant ***R(λ)***, given in Table 8 for each detector.

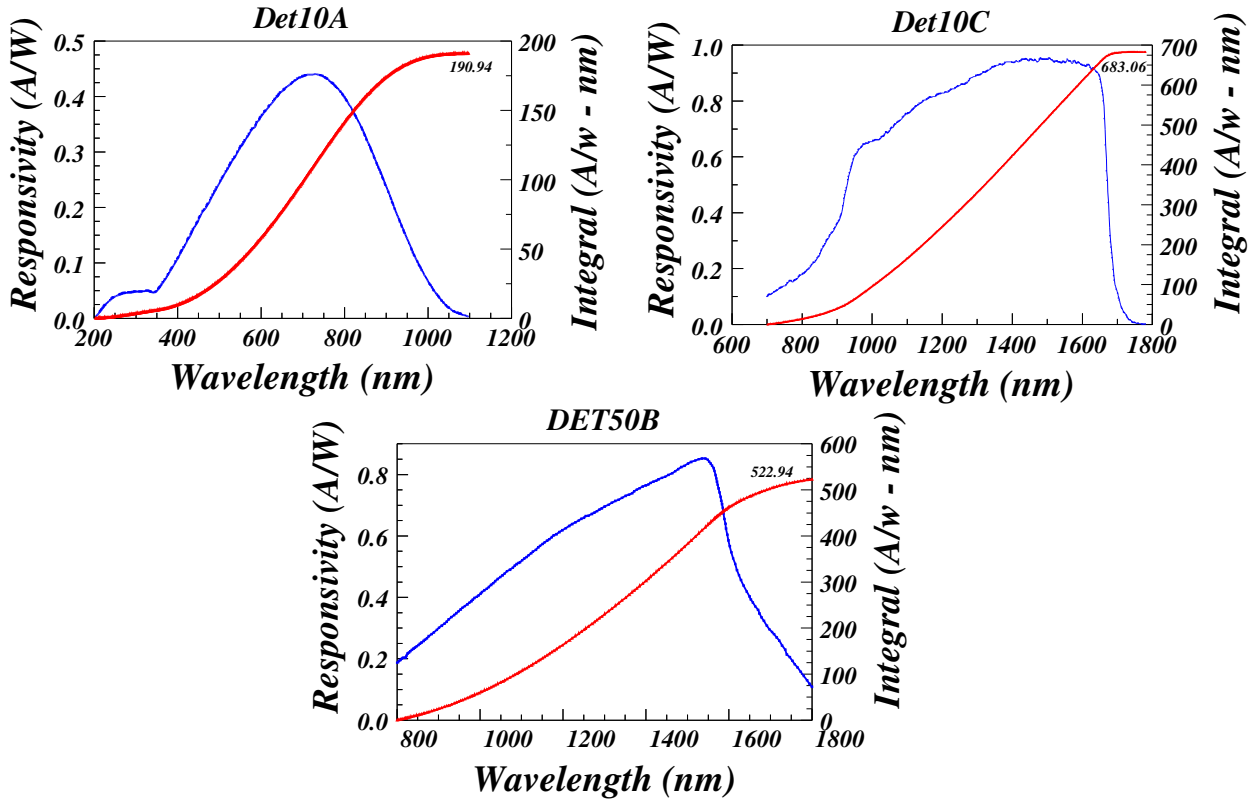

Figure 34. Manufacturer's spectral response curve (in blue) for all diodes used in prompt flash and temperature array diode systems. The spectral response constant R(λ) is determined from integrating the manufacturer's curve (in red) over the detectors wavelength.

The digitized impact flash records are corrected for the -3 db attenuation resulting from the use of 50 power divider and digitizer input loads. The corrected voltage trace (V_{diode}) from equation 19, was converted to photo diode anode current (I_{diode}) by dividing by the series/parallel load resistance (R_{load} = 50) seen by the photo diode, as shown in equation 20. Equation 21 gives the normalized power, dividing by the diodes active area (A_{diode}), to incident power, W/cm^2, on the photo diode over the detector wavelength range. This calibration sequence allows a direct comparison of electromagnetic radiation for each of the detectors spectral response (DET10A, DET10C and DET50B).

$$V_{diode} = \frac{V_{out}}{10^{(\frac{-3}{10})}} \qquad \textbf{(19)}$$

$$I_{diode} = \frac{V_{diode}}{R_{load}} \quad \textbf{(20)}$$

$$P = I_{diode} \frac{(R(\lambda))^{-1}}{A_{diode}} \quad \textbf{(21)}$$

Temperature Array Diode Calibration

The calibration methodology for the temperature array diodes will be different than the prompt flash system, though the basic parameters of the diodes will be used and are described in the diode setup section, 6.2.1. The same 1000 W FEL (used to calibrate the spectrometer in Figure 23) calibration lamp was used to provide a near blackbody spectral source for calibrating the diodes. Again, for our purposes, the blackbody approximation is adequate.

As previously mentioned, the temperature array is comprised of four (4) diodes, three of which are the DET10A silicon diodes and the fourth is a DET10C InGaAs. These broadband diodes are fitted with band pass filters of 340, 460, 600, and 880 nanometers (nm), respectively. These diodes have a given responsivity in amp/watt (A/W) at each of those wavelengths of 0.05, 0.20, 0.36, and 0.33 respectively. These values can be extracted from the calibration curves shown in Figure 34. From Figure 23 and at each of the diode wavelengths, we obtain radiance values for a 3192.4 K blackbody of 4, 32, 83, and 135 milliwatts/m^2 (mW/m^2). Relative to the 600 nm line, the relative radiance values are 0.0548, 0.384, 1.0, and 1.62 respective to each diode wavelength.

Up to this point, calibrations of the diode have been strictly deduced from the manufacturers supplied data. Calibrations on actual diodes are performed for virtually the same reason as spectrometers and that is to take into account the response of the diodes under exact conditions of the experiment. Therefore, the calibrations had to be done with a 1 MΩ terminating resistor to get any kind of voltage out of the detectors that were placed 1.1 m from the FEL lamp and a ~1 cm diameter aperture. (During the experiments, 50 Ω resistors are used.) The signals from the calibration lamp are given in Table 9.

Table 9. KAPF-1 Photo Diode Calibration

Wavelength (nm)	signal into 1MΩ (mV)	signal/responsivity	normalized to 600 nm	blackbody
340	0.72	14.4	0.11	0.055
460	8.0	40.0	0.31	0.384
600	46.41	128.9	1.0	1.0
880	2100.0	6363.6	49.4	1.62

Table 9, column 3 adjusts the measured signal for the responsivity, A/W, of the detector, so that the signals may be compared directly. After this adjustment, the relative sizes of the signals are compared in column 4. Column 5 gives the expected ratios for a blackbody source.

This calibration sequence was performed three times and given that the calibration was done with the same physical layout, the variability in absolute signal is fairly large. The UV signal at 340 nm is mostly noise, and the InGaAs detector is consistently way too big, but at least the ratio to the 460 and 600 nm silicon detector signal is relatively constant. An estimate of the signal can be made from the detector specifications. At 600 nm we have 0.0838 W/cm^2 nm sr from the lamp. The solid angle is 7.85e-7 m^2 / 1.14^2 m^2 = 6.04e-7. The lamp source is approximately 0.785 cm^2 (~1 cm dia hole), and we have a 10 nm bandwidth filter, giving 3.97e-7 Watts into the detector. Assuming 50% transmission and a sensitivity of 0.36 A/W, we expect a photocurrent of 72 nA. This would produce a 72 mV signal into 1 MΩ, so the actual signal, 46 mV, is in the right ballpark, with our estimate of the source area being the most suspect. Something is not right about the 880 nm signal with the InGaAs detector. At 880 nm we have 0.33 A/W. The blackbody gives 0.1355 W/cm^2 nm sr. Using the same solid angle and estimated source area we predict a 106 mV signal, not a 2.1 V signal.

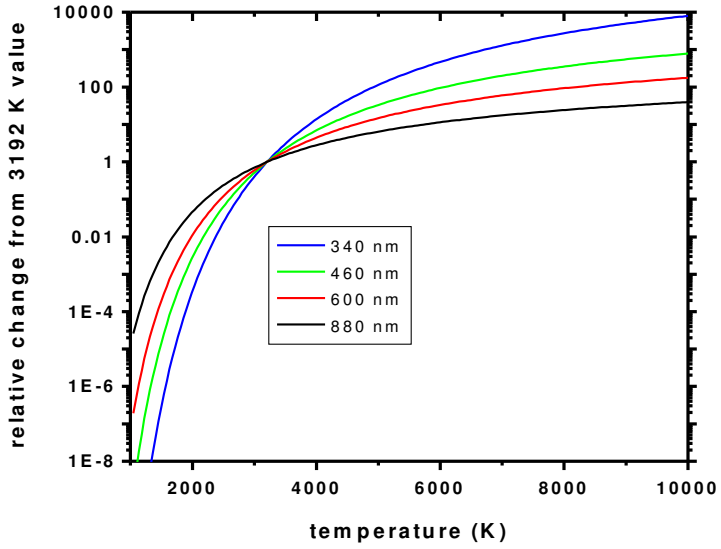

Figure 35. Diode detector sensitivity to temperature normalized to tungsten lamp temperature at 3192 K.

The hope was to use the average signals from the three calibration runs (described above) to make absolute calibration charts for temperature versus signal. However, the calibration data that was performed for our diodes produced too much scatter and the calibration curves proved to be unrealistic. Figure 35 shows the *expected* normalized change in each of the photodiode

signals as a function of temperature from the preset W calibration lamp. Higher sensitivity is represented with a steeper slope. The shift to the blue spectrum is more sensitive at higher temperatures while the shift to the red spectrum is evident at lower temperatures. Note that signals are expected to change over many decades for a one decade change in temperature at any wavelength. For example, if the impact flash is the same ~1 cm diameter area as the lamp and the emission temperature is 10,000 K, then the 340 nm signal is expected to increase by a factor of 10^4. The 1 mV calibration signal into 1 MΩ would turn into a 0.5 mV signal into 50 Ω. This assumes that the impact flash from the radiating body has the same area as the lamp aperture, which may not be true.

6.3. Diode Results

In this section we demonstrate the use of broad band diodes both in the visible and infrared regimes to characterize prompt impact flash light signatures and to observe *late time* events (expanding and radiating debris clouds after initial impact). We have successfully demonstrated the use of diodes as a tool to observe and characterize the two afore mentioned scenarios. In addition, silicon diode measurements at four specific wavelengths have been used as a pyrometer to estimate the temperature of a hypervelocity impact.

Table 10 describes the experimental set ups for the various experiments where silicon diode diagnostics have been used to observe and characterize the prompt impact flash light signatures as well as radiating debris clouds.

Table 10. Experimental setup for diode experiments

Shot Nos.	IV (km/s)	Flyer Plate Material/Thk. (mm)	Target Material/Angle/Thk. (mm)	Diagnostics	Config.
KAPF-1	7.35	Ti6Al4V / 0.90	Al / 0° / 1.0	Prompt Flash / Temp. Array[1]	Figure 16
KAPF-3	10.90	Ti6Al4V / 0.90	Al / 20° / 1.0	Prompt Flash / Temp. Array[1]	Figure 16
KAPF-6	9.30	Ti6Al4V / 0.90	Al / 20° / 1.0	Prompt Flash	Figure 16
KAPF-7	7.30	Ti6Al4V / 0.90	Al / 20° / 1.0	Prompt Flash	Figure 16
THZ-1	5.59	Lexan / 37	Comp-B / 0° / 5.1	THz / RDS[2]	Figure 14
THZ-2	7.04	Lexan / 37	Comp-B / 0° / 5.1	THz / RDS[2]	Figure 14
THZ-3	7.68	Lexan / 25	Comp-B / 0° / 5.1	THz / RDS[2]	Figure 14

[1] Temperature array is located 940 mm from inclined target and 318 below flight path.

[2] Tera-Hertz and radiating debris system diagnostics

6.3.1 Scaling Laws for Comp B.

In this section, we will report the results of the impact flash signatures (integrated over their respective broad band ranges) both by the visible and the Near IR diodes. The experimental configuration is shown in Figure 14. Notice that the diode probes are observing the back side of the target and not the impact side. The diodes observe the radiance emitted by the shocked and subsequent expanding Comp-B as it propagates down stream. The results of the visible radiance as recorded by the silicon diodes are shown in Figure 36 (a) as a function of impact velocity over the range of 5.5 to 7.7 km/s. The impact conditions are reported in Table 4 in Chapter 4.2 and Table 10 above. Likewise the NIR signatures from the germanium diode out put are shown in Figure 36 (b) as a function of impact velocity. As indicated in Figures 36 (a) and (b), there is an increase in luminosity for approximately over the first 0.5 μs, before the signal decreases to an equilibrium value. The former is a result of shock propagation through the Comp-B sample. The luminosity decreases as the shock reflects of the free surface. The peak luminosity results from the shocked sample while the equilibrium value results from the released state.

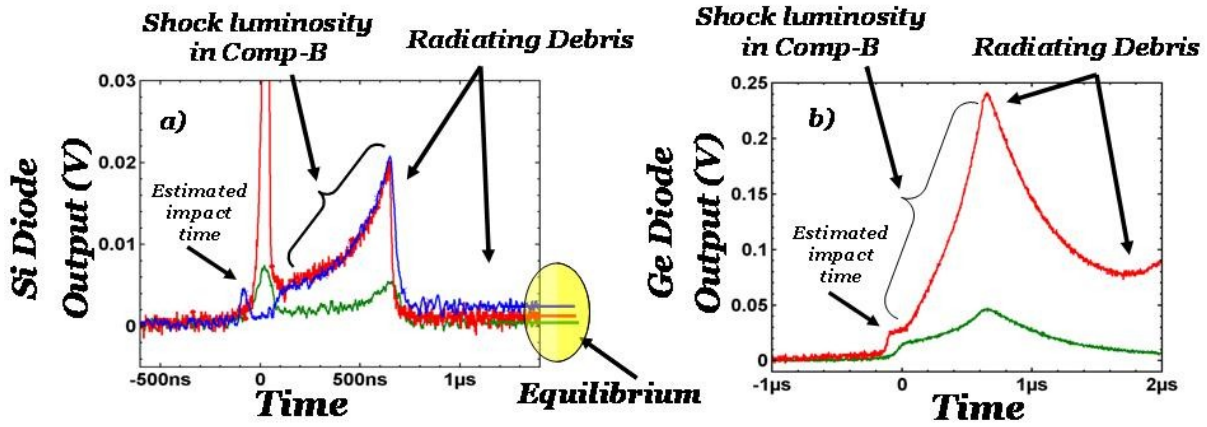

Figure 36. Diode signals converted to normalized power (recording circuit, spectral response curve) Diodes directly viewing rear of comp-b target. Luminosity scaling factor of 0.55 to 0.83 observed as a function of impact velocity. Data signals in both (a) and (b) show impact time estimate with increasing luminosity as shock propagates through Comp-B, reflects from rear surface(at the peak) followed by the released states decreasing in luminosity. Diode signals in (a) are the DET10A described in Table 8, for experiments THz-1,2 and 3. Diode signals in (b) are the Ge Diodes described in Table 8 for experiments THz-1, 3 (Diode in THz-2 failed).

The peak luminosity can be converted to obtain the power per unit area as described above. Plots of radiative power as a function of impact velocity is shown in Figure 37 obtained both for the visible and near IR diodes as a log plot. The slope of this line which varies form 0.55 to 0.83 yields the scaling laws for the radiative emission spectrum over these wavelength regimes. The scaling law suggests wavelength dependence from the visible spectrum to the NIR spectrum

regime. There is also time dependence to this signature suggesting a different response from the shocked state to the equilibrium released state. Further studies are, however, needed to verify this phenomenology. In this study, the scaling law is described as a function of impact velocity. Since the target material (Comp-B) and the impactor material (Lexan) remain the same in all experiments, it should be a good predictor of radiative emission vs impact velocity for Comp B as long at the impactor is Lexan. If other materials were used as an impactor then it would be prudent to describe the luminosity variations as a function of shock parameters such as peak pressure, particle velocity or temperature in Comp B.

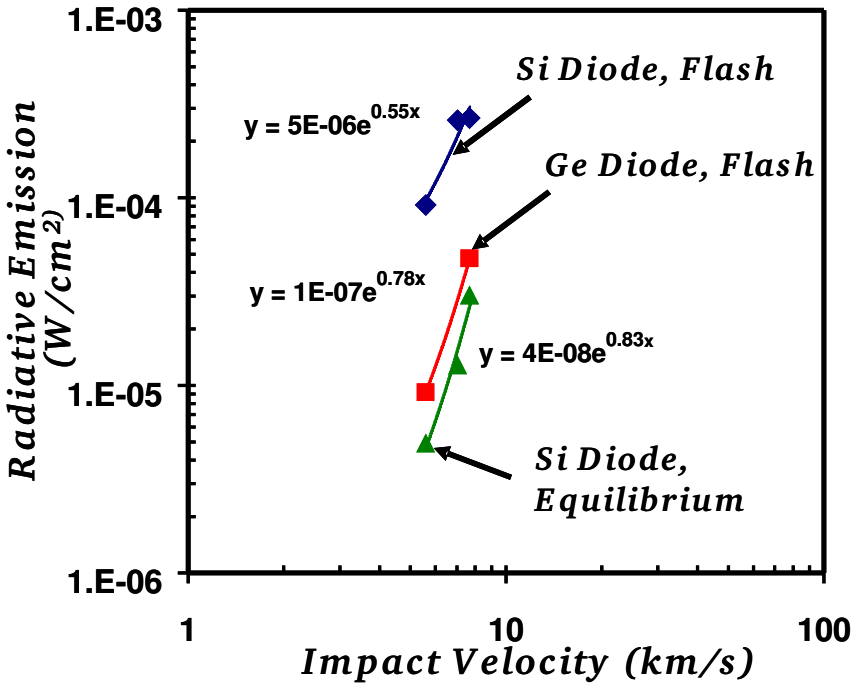

Figure 37. The peak luminosity is converted to obtain the power per unit area as described in the above plot. Radiative power as a function of impact velocity obtained both for the visible and near IR diodes as a log plot. The slope of this line which varies form 0.55 to 0.83 yields the scaling laws for the radiative emission spectrum over these wavelength regimes.

6.3.2 Scaling Laws for Aluminum

To obtain the scaling laws for aluminum we used the experimental impact configuration indicated in Figure 16 (See Chapter 3). A titanium flier plate impacts an aluminum target plate which is obliquely placed at 20 degrees from its vertical axis. This is shown in Figure 16 as well. This set up was used to observe the impact flash radiative signals as observed at the impact surface. This is also referred to as prompt flash signatures by some researchers. Only silicon diodes were used in this study. A pyrometer diode arrays are also used in this study and is positioned to observe the impact surface. The impact conditions are given in Table 10.

As indicated in the Table 10 (KAPF shots), the experiments were conducted over an impact velocity range from 7 to 11 km/s. The output of the silicon diodes signatures are shown in Figure 38 (a) for the experiments given in Table 10. Time, t=0 equals impact time of titanium impact with the aluminum plate. Notice that the luminosity is considerably intense for the 11 km/s than for the experiments performed at approximately 7 km/s. The variation of emission intensity as a function of impact velocity is shown plotted in Figure 38 (b). Only the peak estimates are shown as a log plot. Since you are observing the impact surface in this experiment, it is not clear if you are observing the radiative emission from the titanium impactor or from the aluminum target especially at late times. The scaling law, however, gives a systematic variation with an exponent of 1.3. In all likelihoods it is for aluminum since these estimates are for given for early times, and titanium will not be shielding the aluminum interface. However it is not clear if the late time temperature estimates given in the next section represents the temperature of the titanium impactor after impact or the aluminum debris plate generated upon impact. This is discussed in the next section.

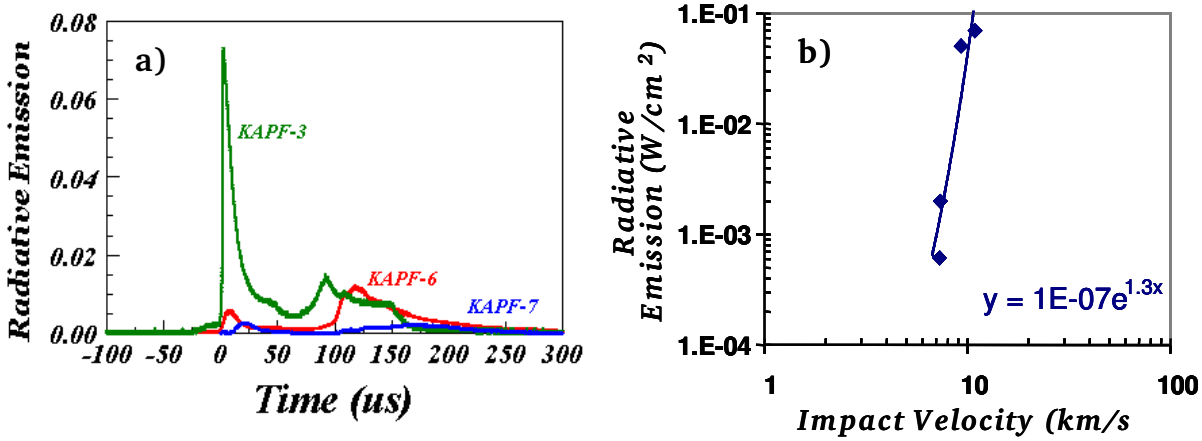

Figure 38. The variation of emission intensity as a function of impact velocity is shown above. The silicon diodes signatures are shown in (a). In (b), only the peak estimates (radiative emission) are shown.

6.3.3 Temperature Estimates

We will use the data acquired from KAPF-3, the highest velocity experiment as the signals were much larger. The temperature array diode (described in section 6.2.1 and located according to Table 10) light signatures are shown in Figure 39 (a) and (b). A titanium flyer impacts the aluminum plate (configuration shown in Figure 16 and described in Table 10) at approximately 252 μs and the impact is recorded by the diodes in Figure 39. The first thing to note is that the signals are considerably larger than would be expected from a 10,000 K surface with the same area as the calibration lamp. The 340 nm signal peaks with a 30 mV signal, 60 times bigger than expected. Either the temperature of impact is considerably higher than 10,000 K or the effective

area of the flash as seen by the detector is considerably larger. The larger area is the most likely possibility.

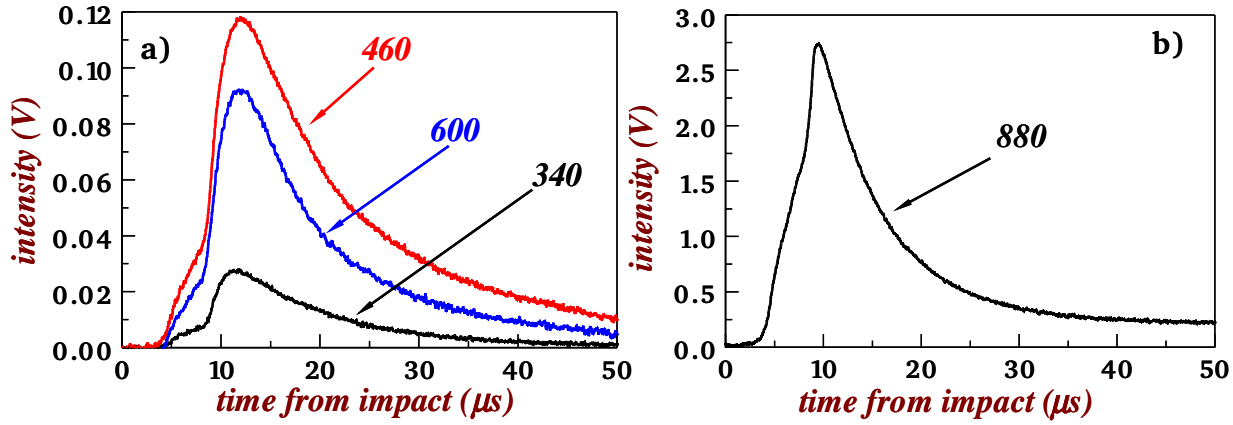

Figure 39. The diode data signatures in the above figure represent impact of the flyer on an aluminum plate at 252 μs. Each diode is covered by a 10 nm band pass filter 340, 460, 600 nm for the visible silicon diodes and 880 nm for the NIR InGaAs diode.

The signals in figure 39 are roughly the same shape, implying that we may possibly use ratios of signals to back out a two-color temperature for each pair of waveforms at each time. First, extract signals, assuming the baseline is zero, ignoring the small rise in signal before impact. We then adjust the signal values for spectral sensitivity, 0.05, 0.2, and 0.36 in the case of 340, 460 and 600 nm, respectively. For each pair of wavelengths, we may extract a graybody ratio temperature from

$$\frac{1}{T}=\frac{\lambda_1\lambda_2}{c_2(\lambda_2-\lambda_1)}[\ln(s_2/s_1)+5\ln(\lambda_2/\lambda_1)] \qquad \textbf{(22)}$$

To properly take this ratio, we need to interpolate each data file such that the y values correspond to the same common x value.

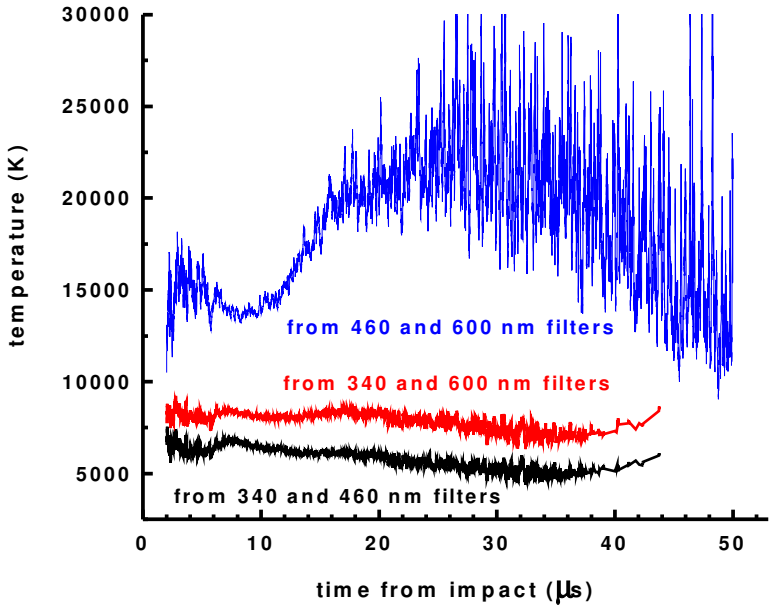

Figure 40. Computed graybody ratio temperatures for all pairs of silicon detectors.

Figure 40 shows the computed graybody ratio temperatures for all pairs of silicon detectors. One would expect a dramatic rise and fall in temperature similar to the pulse recorded by each detector, however the temperature estimates are practically constant. The logical assumption is that the diodes are monitoring essentially a liquid plate and since the dimensions of the "liquid-plate" would be finite, the cooling process would take considerably more time. Some temperatures seem reasonable, 7000 K, but the temperature spread between different possible choices of detector pairs indicates that the calculated ratio temperatures are probably not meaningful. Note that we cannot determine the temperature at all times with the ratio method. It is only possible to determine a temperature when both signals have measurable signal intensity.

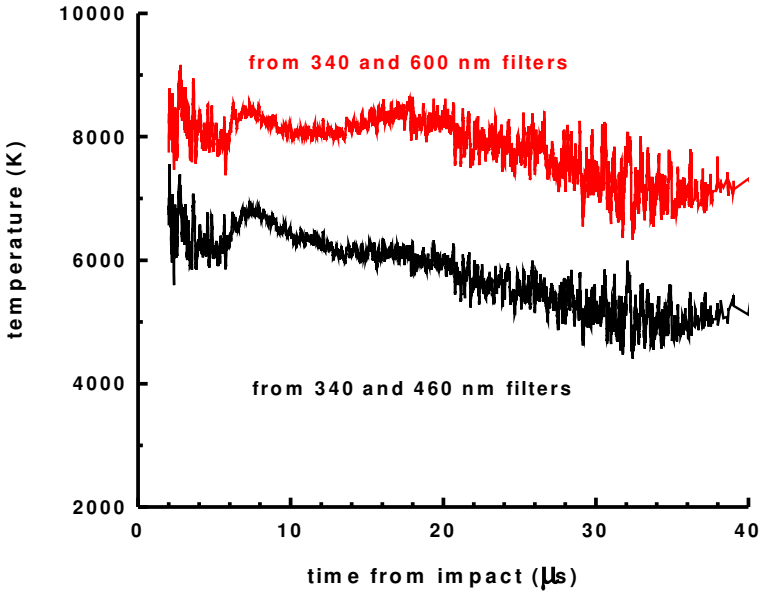

Figure 41. Computed graybody ratio temperatures for biased pairs of silicon detectors.

If we reject the 460 and 600 ratio temperature data as being too high, we obtain the admittedly biased sets of data above. These have been retained only because they seem more reasonable, but there is no way to prove that this is not just a coincidence at this time. Even though the temperature estimates are high, they are not unreasonable considering that the shock-induced vaporization process is a time-dependent phenomenon. It has been shown in a previous study that the impact generated aluminum debris traverses as a molten plate for over 75 microseconds. Since the emission is observed from a finite sized body it is not expected to cool very rapidly.

We conclude that the 11 km/s impact flash is putting out a tremendous amount of light for a very brief time – thousands of times more than the 1 kW calibration lamp. Temperature is harder to determine. To use each detector as a single-wavelength pyrometer would require some spatial resolution, perhaps with a lens and aperture combination. The spatial extent of the flash would then no longer be a consideration. We would be measuring the temperature of a small spot in the flash region. However, it is still possible that this emission is not blackbody and it would still be difficult to extract a meaningful temperature.

7. CONCLUSIONS

To summarize, this study may be best characterized as new technology development which can lead to the implementation of new sensors for use in investigating the optical characteristics of a rapidly expanding debris cloud that result from hypervelocity impact. In particular, this project expanded the diagnostics for dynamic spectroscopy at our gas-gun facility from the visible and infrared into the THz region of the spectrum. Our gas guns constitute a unique test bed that provides well-controlled experimental environments that match operational conditions relevant to hypervelocity impact such as those encountered in space engagements.

Extending our impact-flash spectral measurements into the THz regime allowed us to perform tests and analysis in this new spectral regime, which is complementary to our current capabilities in the visible and infrared. THz spectroscopy may potentially offer significant advantages, in particular, the THz region is less crowded, and will still be emitted by molecules that have cooled too much to emit in the infrared. THz spectra relate to molecular motions, some of which have been cataloged for operational materials of interest. The combined capabilities would offer a much broader range of material identification possibilities and complement/verify those achievable with the atomic measurements provided by visible and infrared spectroscopy alone. More significantly, these combined technologies now have the potential of identifying the dissociation or reaction products of many systems that has undergone a high velocity impact and deformation. To begin exploring the usefulness of applying THz technology to understand impact phenomenology, this LDRD effort provided new measurement and recording systems appropriate for THz investigations in these dynamic environments. In addition, we further enhanced existing visible and near-infrared capabilities.

This study also complemented the spectroscopic measurements by obtaining temperature estimates of the impact generated debris that results from high velocity engagements. The impact generated debris is time-dependent in that its transport/expansion behavior is changing with time. The rapid expansion behavior of the debris is expected to “cool” the cloud rapidly, thus changing its thermal characteristics with time. The test methodology consisted of fitting the debris emission spectrum to a blackbody radiation function even though the debris cloud may not be in thermodynamic equilibrium.

In this study we have implemented new sensors for use in investigating the optical characteristics of a rapidly expanding debris cloud that results from hypervelocity impact. We have demonstrated the use of (1) terahertz sensors, (2) silicon diodes for visible regimes, (3) germanium and InGaAs sensors for the near infrared regimes, and (4) the Sandia lightning detectors which are similar to the silicon diodes described in 2. The combination and complementary use of all these techniques has the strong potential of “thermally” characterizing the time-dependent behavior of the radiating debris cloud.

A variety of sensors that span over a wide spectrum, varying from visible regime to THz frequencies, gives us the potential to characterize the impact over a broader temporal regime starting from high-pressures (Mbar) high-temperatures (eV) to low pressures (mbar) low temperature (less than room

temperature) as the debris expands and cools. In addition the broad frequency coverage enables one to improve determination of the cloud constituents and dynamics by exploring multiple phenomenologies.

Results of this study maybe highlighted as follows:

1. A simple model of the temporal dynamics and spectral characteristics of the THz emission from an expanding vapor cloud has been developed.
2. THz emission from impact debris has been successfully demonstrated. As THz technology develops, spectroscopic identification will become possible which could be explored with new measurements.
3. Silicon diodes can be used in the visible regime both in a broad band regime or as a narrow band spectrometer at specific wavelengths to determine its time-dependent radiation emission with nanosecond time resolution.
4. Silicon diode measurements at four specific wavelengths have been used as a pyrometer to estimate the temperature of the expanding and radiating hypervelocity impact-generated debris. Further experiments with better spot size definition may improve the accuracy of temperature estimates.
5. Temperature estimates were also determined using the results of optical emission data recorded by the multi-channel analyzer both in the visible and near infra-red regime.
6. Temperature estimates for Comp-B are much higher than expected or estimated based on the assumption that the debris cloud is expanding as an ideal gas.
7. Sandia lightning detectors were also used in some experiments to measure the broad band radiation in the visible regime. It is not unlike the silicon diodes in that it had a “larger” detection area compared to the silicon diode mentioned above with the sampling rate of a microsecond.

The results reported in this study are extremely encouraging. It is our belief that we have conclusively demonstrated the technologies described above will characterize the impact generated debris a lot more thoroughly than it has ever been attempted heretofore. It is now possible to diagnose the debris characteristics mechanically to obtain its expansion and transport properties, optically over a wide frequency regime (from visible spectrum frequencies to terahertz frequencies) to estimate its electromagnetic spectral properties, and also thermally to obtain the time dependent temperature states as the debris cool upon expansion. Incidentally, these are also some of the first steps necessary to obtain the physical properties of warm dense matter. Further research is necessary not only to improve and increase the precision of the diagnostic capabilities reported herein but also to use it in characterizing strategic materials of interest to the technical and scientific community.

8. REFERENCES

1. *Infrared System Engineering*, R.D. Hudson, p50-53, John Wiley and Sons, NY (1969).

2. *Physics of Shock Waves and High-Temperature Hydrodynamic Phenomena*, Ya. B. Zeldovich and Yu. P. Raizer, section 28, Academic Press, NY (1966).

3. *Unsteady Motions of Continuous Media*, K. P. Stanyukovich, Academic Press, NY (1960).

4. *Infrared Detectors and Systems*, E.L. Dereniak and G.D. Boreman, p.55, John Wiley & Sons, NY (1996).

5. The commercial composite silicon and niobium bolometers were supplied by QMC instruments Ltd. (www.terahertz.co.uk).

6. Description of the plasmon detector can be found in (i) "Terahertz photoconductivity and plasmon modes in double-quantum-well field-effect transistors", X.G. Peralta, et al., *Appl. Phys. Lett.,* 81, 1627 (2002),(ii) "Single-quantum-well grating-gated terahertz plasmon detectors ", E.A. Shaner, et al., *Appl. Phys. Lett.,* 87, 193507 (2005), (iii) "Millimeter wave mixing using plasmon and bolometric response in a double-quantum-well field-effect transistor", M, Lee, et al., *Appl. Phys. Lett.,* 86, 033501 (2005), and (iv) "Far-Infrared Spectrum Analysis Using Plasmon Modes in a Quantum-Well Transistor", E.A. Shaner, et al., *IEEE Phot. Tech. Lett*., 18, 1925 (2006).

7. ThorLabs Inc., "DET10A Operating Manual - High Speed Silicon Detector," Document No. 13052-S01 Rev A (ThorLabs Inc.) pp. 1-5, 2006.

APPENDIX A KALIEDAGRAPH SCRIPT

This script took the output of the HITRAN code which had two columns (the wavenumber in cm^{-1}, and the absorption coefficient, α in dB/meter) and calculated the spectral spectral total attenuation, effective emissivity, spectral radiance, and the spectral and integrated flux hitting the detector.

```
m1 = 65;  (μs)                                  time
m2 = 6.6*10^-34;    (kg m^2/s)                  h
m3 = 3*10^8;      (m/s)                         c
m4 = 5.66*10^-8;    (W/m^2 K^4)                 Stephan-Boltzman (sigma)
m5 = 1.39*10^{-23};                             k
m6 = 9720* m1^-0.848;  (K)                      Temperature (K)
m7 = .2*.2;    (cm^2)                           effective  detector area
m8 = 33;         (gram)                         mass of Comp-B
m15 = 0.00615; (m/microsec)                     radial expansion velocity
m9 = m15 * m1;  (m)                             radius of gas ball
m10 = .031 * m8;   (moles)                      moles of gas of byproducts
;              CompB has 31.4 moles/kg
m11 = 8.314*10^{-2};  (J/mol K * 10^-2)         Gas constant, R, converted to give mbars
m12 = m10*m11*m6/((4/3)*3.14*m9^3);             pressure (p = nRT/V) in mbar
m13 = 2;                                        F/# of collecting lens
m14 = .0006*6.28*100; (m^-1)                    linewidth
m16 = 0.292;  (m)                               distance downstream from impact to optical path
m17 = 0.0046;  (m/microsec)                     center of mass velocity
m18 = 2 ((m15*m1)^2 - (.292-m17*m1)^2)^1/2;  (m)  optical path length
;
; c0 = wavenumber (cm-1)
name("Freq (cm\ u-1\ n)",c0);
;
; c1 = frequency (THz)
c1 = c0 * .030;
name("Freq (THz)",c1);
;
; c2 = frequency (Hz)
c2 = c1 * 10^{12};
name("Freq (Hz)", c2);
;
```

```
; c3 = attenuation (dB/meter/mbar)
name("Attenuation (dB/m/mbbar)", c3);
;
; c4 = attenuation (dB)
; c4 = att (dB/m/mbar) * opticalpathlength (m) * pressure (mbar)
c4 = -c3*2*m9*m12;
name("Attenuation (dB)",c4);
;
; c5 = emissivity
c5 = 1-10^(c4/10);
name("Emissivity", c5);
;
; c6 = L_e = spectral radiance of blackbody   watt / m^2-sr-m^-1
c6=((6.28*100*c0)^3*m2*m3^2)/((8*(3.14)^4)*(exp( (m2*m3*6.28*100*c0)/
     (2*3.14*m5*m6) )-1))* m14;
name("BB Spectral Radiance", c6);
;
; c7 = "spectral radiance of gas"   watt / m^{2}-sr
; note if c6 was defined normally, we would have to multiply
; by the linewidth(m14).
; However, renormalizing above, rescaled dk.
; Radiance = emissivity*spectralradiance
c7 = c5*c6;
name("Binned Gas Spectral Radiance", c7);
;
;c8 = Radiance, L = spectral radiance integrated from 0 cm-1 to x cm-1.
c8 = rsum(c7);
name("Radiance (0-x cm-1)", c8);
;
;c9 = Irradiance, E = pi*L / [4(F/#) + 1]  (Watt / cm^{2})
c9 = 3.14*c8 / (4*m13+1);
name("Irradiance", c9)
;
;c10 = flux (watts) = E * detector area
c10 = c9 * m7;
name("Flux on detector", c10);
;
cell(0,12) = m6;   Temp
```

```
cell(1,12) = m12;  Pressure
cell(2,12) = m7;   Detector Area (cm-2)
cell(3,12) = m14;  linewidth (m-1)
cell(4,12) = m8;   mass of Comp-B
cell(5,12) = m13;  F/# of collection optics
cell(6,12) = m9*2; pathlength of gas
;
;c13 = Irradiance, E = pi*L / [4(F/#) + 1]  (Watt / cm^{2})
c13 = 3.14*c7 / (4*m13+1);
name("spectral Irradiance", c13)
;
;c14 = flux (watts) = E * detector area
c14 = c13 * m7;
name("spectral Flux on detector", c14);
```

APPENDIX B ABSORPTION LINE INPUT FILES

B.1 HITRAN Input Files

The following is the LNFL input file that was used in this work. These select the subset of the HITRAN database that is to be used with the LBLRTM and writes a data file in the required format.

```
lnfl input file for range of 0 cm-1 to 400 cm-1 with CompB prods
0.     400.
1100111101000000000101000010000000000001          NBLK1 LNOUT
%%%%%%%%%%%%%%%%%%%
```

B.2 Low-resolution LBLRTM input files

The following are the input files for the various runs of the LBLRTM program along with notes where variations were used.

The following is the TAPE5 input file for low-resolution, P=1mb and T=70K data set. A similar input file was also used for the 100K, 278K and 1000K model runs.

```
$ Input file for lblrtm looking at absorption effects of CompB prods.
 HI=1 F4=1 CN=1 AE=0 EM=1 SC=1 FI=0 PL=0 TS=0 AM=1 MG=0 LA=0 OD=0 XS=0   00   00
0.00       400.00                                0.0002    0.001
0.0
   0    1    0    1    1   27   1 0  0     0.000     0.000                19
   1.524                 0.001
   1      Single layer model with all the CompB prods availible in the database
   -1.524 1.000E+0  0.700E+2      AA L AAAAAAAAAAAAAAAAAAAAAAAAAA
3.97496105E+05    1.93938605E+05    0.00000000E+00    0.00000000E+00    6.61856496E+04    9.40231172E+01
2.15628897E+01 1.87441072E+02
0.00000000E+00    5.14706495E-08    0.00000000E+00    0.00000000E+00    0.00000000E+00    0.00000000E+00
0.00000000E+00 0.00000000E+00
0.00000000E+00    0.00000000E+00    0.00000000E+00    6.38287015E-01    0.00000000E+00    3.42075975E+05
0.00000000E+00 0.00000000E+00
0.00000000E+00 0.00000000E+00 3.60867858E-05
0.0100     1.0      400.0         0   0    1
-1.
$ Transfer to ASCII plotting data
 HI=0 F4=0 CN=0 AE=0 EM=0 SC=0 FI=0 PL=1 TS=0 AM=0 MG=0 LA=0 MS=0 XS=0    0    0 \\
```

```
# Plot title not used
  3.0      350.0       10.2000  100.0000    5    0   11    0     1.000 0  0    0
   0.0000    1.2000    7.0200    0.2000    4    0    1    0    0    0 0    3 27
  3.0      350.0       10.2000  100.0000    5    0   11    0     1.000 0  0    0
   0.0000    1.2000    7.0200    0.2000    4    0    1    0    2    0 0    3 28
-1.
%%%%%
```

The following is the TAPE5 input file for low-resolution, P=10mb and T=70K data set. A similar input file was also used for the 100K, 278K and 1000K model runs.

```
$ Input file for lblrtm looking at absorption effects of CompB prods.
 HI=1 F4=1 CN=1 AE=0 EM=1 SC=1 FI=0 PL=0 TS=0 AM=1 MG=0 LA=0 OD=0 XS=0   00   00
0.00       400.00                                  0.0002    0.001
0.0 \\
   0    1    0    1    1   27   1 0  0     0.000     0.000                  19
   1.524                  0.001
   1      Single layer model with all the CompB prods availible in the database
   -1.524 1.000E+1  0.700E+2      AA L AAAAAAAAAAAAAAAAAAAAAAAAAA
3.97496105E+06    1.93938605E+06    0.00000000E+00    0.00000000E+00    6.61856496E+05    9.40231172E+02
2.15628897E+02 1.87441072E+03
0.00000000E+00    5.14706495E-07    0.00000000E+00    0.00000000E+00    0.00000000E+00    0.00000000E+00
0.00000000E+00 0.00000000E+00
0.00000000E+00    0.00000000E+00    0.00000000E+00    6.38287015E-00    0.00000000E+00    3.42075975E+06
0.00000000E+00 0.00000000E+00
0.00000000E+00 0.00000000E+00 3.60867858E-04
0.0100     1.0      400.0         0   0    1
-1.
$ Transfer to ASCII plotting data
 HI=0 F4=0 CN=0 AE=0 EM=0 SC=0 FI=0 PL=1 TS=0 AM=0 MG=0 LA=0 MS=0 XS=0    0    0
# Plot title not used
  3.0      350.0       10.2000  100.0000    5    0   11    0     1.000 0  0    0
   0.0000    1.2000    7.0200    0.2000    4    0    1    0    0    0 0    3 27
  3.0      350.0       10.2000  100.0000    5    0   11    0     1.000 0  0    0
   0.0000    1.2000    7.0200    0.2000    4    0    1    0    2    0 0    3 28
-1.
%%%%%
```

The following is the TAPE5 input file for low-resolution, P=100mb and T=70K data set. A similar input file was also used for the 100K, 278K and 1000K model runs.

```
$ Input file for lblrtm looking at absorption effects of CompB prods.
 HI=1 F4=1 CN=1 AE=0 EM=1 SC=1 FI=0 PL=0 TS=0 AM=1 MG=0 LA=0 OD=0 XS=0   00   00
0.00       400.00                                  0.0002    0.001
```

```
0.0
   0    1    0    1    1   27   1 0  0     0.000     0.000                 19
   1.524                 0.001
   1      Single layer model with all the CompB prods availible in the database
   -1.524 1.000E+2  0.700E+2      AA L AAAAAAAAAAAAAAAAAAAAAAAAAAA
3.97496105E+07    1.93938605E+07    0.00000000E+00    0.00000000E+00    6.61856496E+06    9.40231172E+03
2.15628897E+03 1.87441072E+04
0.00000000E+00    5.14706495E-06    0.00000000E+00    0.00000000E+00    0.00000000E+00    0.00000000E+00
0.00000000E+00 0.00000000E+00
0.00000000E+00    0.00000000E+00    0.00000000E+00    6.38287015E+01    0.00000000E+00    3.42075975E+07
0.00000000E+00 0.00000000E+00
0.00000000E+00 0.00000000E+00 3.60867858E-03
0.0100     1.0      400.0         0   0    1
-1.
$ Transfer to ASCII plotting data
 HI=0 F4=0 CN=0 AE=0 EM=0 SC=0 FI=0 PL=1 TS=0 AM=0 MG=0 LA=0 MS=0 XS=0    0    0
# Plot title not used
  3.0      350.0       10.2000  100.0000    5    0   11    0     1.000 0  0    0
    0.0000    1.2000    7.0200    0.2000    4    0    1    0    0    0 0    3 27
  3.0      350.0       10.2000  100.0000    5    0   11    0     1.000 0  0    0
    0.0000    1.2000    7.0200    0.2000    4    0    1    0    2    0 0    3 28
-1.
%%%%%
```

B.3 High-Resolution LBLRTM Input File Example

The following is the TAPE5 input file for high-resolution work, specifically for the T=70k and P=1mb data set. Similar files were used for the other data sets.

```
$ Input file for lblrtm looking at absorption effects of CompB prods.
 HI=1 F4=1 CN=1 AE=0 EM=1 SC=1 FI=0 PL=0 TS=0 AM=1 MG=0 LA=0 OD=0 XS=0   00   00
0.00       400.00                                0.0002    0.001
0.0
   0    1    0    1    1   27   1 0  0     0.000     0.000                 19
   1.524                 0.001
   1      Single layer model with all the CompB prods availible in the database
   -1.524 1.000E+0  0.700E+2      AA L AAAAAAAAAAAAAAAAAAAAAAAAAAA
3.97496105E+05    1.93938605E+05    0.00000000E+00    0.00000000E+00    6.61856496E+04    9.40231172E+01
2.15628897E+01 1.87441072E+02
0.00000000E+00    5.14706495E-08    0.00000000E+00    0.00000000E+00    0.00000000E+00    0.00000000E+00
0.00000000E+00 0.00000000E+00
0.00000000E+00    0.00000000E+00    0.00000000E+00    6.38287015E-01    0.00000000E+00    3.42075975E+05
0.00000000E+00 0.00000000E+00
0.00000000E+00 0.00000000E+00 3.60867858E-05
0.0003     1.0      400.0         0   0    1
-1.
$ Transfer to ASCII plotting data
```

```
 HI=0 F4=0 CN=0 AE=0 EM=0 SC=0 FI=0 PL=1 TS=0 AM=0 MG=0 LA=0 MS=0 XS=0    0    0
# Plot title not used
  3.0      350.0       10.2000  100.0000    5    0   11    0     1.000 0  0    0
    0.0000    1.2000    7.0200    0.2000    4    0    1    0    0    0 0    3 27
  3.0      350.0       10.2000  100.0000    5    0   11    0     1.000 0  0    0
    0.0000    1.2000    7.0200    0.2000    4    0    1    0    2    0 0    3 28
-1.
%%%%%
```

B.4 Atmospheric, 7 Primary Molecules

The following is an example of the input file for seeing what the absorption effective of air leaking into a vacuum vessel for compBprod experiments might look like. The following is the input file used for the 30% relative humidity case.

```
$ Input file for lblrtm looking at absorption effects of 7 stand atm mole 30\% humidity on THz radiation.
 HI=1 F4=1 CN=1 AE=0 EM=1 SC=1 FI=0 PL=0 TS=0 AM=1 MG=0 LA=0 OD=0 XS=0   00   00
0.00       400.00                                0.0002    0.001
0.0
    0    1    0    1    1    7   1 0  0     0.000     0.000                19
    1.524                 0.001
    1      Single layer simplistic model
    -1.524  000.100     278.3      AA L H666666
30
0.01       1.0      400.0         0   0    1
-1.
$ Transfer to ASCII plotting data
 HI=0 F4=0 CN=0 AE=0 EM=0 SC=0 FI=0 PL=1 TS=0 AM=0 MG=0 LA=0 MS=0 XS=0    0    0
# Plot title not used
  3.0      350.0       10.2000  100.0000    5    0   11    0     1.000 0  0    0
    0.0000    1.2000    7.0200    0.2000    4    0    1    0    0    0 0    3 27
  3.0      350.0       10.2000  100.0000    5    0   11    0     1.000 0  0    0
    0.0000    1.2000    7.0200    0.2000    4    0    1    0    2    0 0    3 28
-1.
%%%%%
```

APPENDIX C DETECTOR SETTINGS

Table 10. Detector settings for each THZ shot

	Shot 1	*Shot 2*	*Shot 3*
Si Bol Gain	1000	1000	100
Si Bol ext. filter	-	Flourogold	-
Nb Bol heater voltage (V)	2.4	2.68	
Nb Bol temp sensor voltage (V)	1.681	1.6818	1.6804
Nb Bol resistance (Ω)	5	9.35	10
PD used			751A4
PD Vgd (V)			-0.36
PD Isd (μA)			10.0
PD Vsd (V)			-0.58
PD Vsf (V)			-0.994
PD Temp (K)			20
PD Amplifier			SR560
PD Amp Gain			100
PD Amp Bandwidth (kHz)			1-1000
Beampath purged	No	Yes	Yes

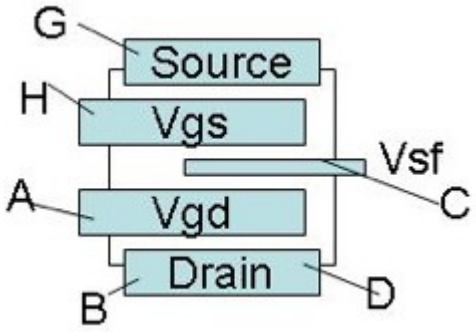

Figure 42. Plasmon Detector Wiring Schematic, showing variables defined in Table 10.

DISTRIBUTION

1	MS0431	Jay Vinson	0510
2	0670	William Breiland	5526
1	0980	Toby Townsend	5703
1	0980	Jay Jakubczak	5710
1	0982	Dan Carroll	5732
1	1071	Andy Boye	1720
1	1079	Gilbert V. Herrera	1700
20	1082	Michael Wanke	1725
2	1082	Albert Grine	1725
2	1082	Michael Mangan	1725
1	1082	Jim Hudgens	1725
1	1161	Terry Stalker	5432
1	1168	Clint Hall	1646
1	1168	Brent Jones	1646
1	1168	Robert Abbott	1647
1	1168	Michael Furnish	1647
1	1168	Dillion Mcdaniel	1650
1	1178	Doug Bloomquist	1630
25	1181	Lalit Chhabildas	1647
10	1181	William Reinhart	1647
10	1181	Tom Thornhill	1647
2	1181	Justin Brown	1646
1	1181	Tom Mehlhorn	1640
1	1181	Larry Schneider	1650
1	1181	Jean-Paul Davis	1646
1	1181	Daniel Dolan	1646
1	1181	Marcus Knudson	1646
1	1181	Jack Wise	1646
1	1181	Tracy Vogler	1647
2	1181	Scott Alexander	1647
1	1185	Bruce Swanson	5410
1	1185	Gregory Bessette	5417
1	1185	Jeromy Hollenshead	5417
1	1185	Dan Kelly	5417
1	1185	Ray Dukart	5417
1	1185	Mehdi Eliassi	5417

1	1185	Robert Weir	5417
1	1185	Susan Goudy	5417
1	1190	Keith Matzen	1600
1	1190	Craig Olsen	1640
1	1191	John Porter	1670
2	1415	Eric Shaner	1123
2	1423	Paul Miller	1128
1	1423	Gregory Hebner	5417
2	MS9018	Central Technical Files	8945-1
2	MS0899	Technical Library	4536
1	MS0188	D. Chavez, LDRD Office	1030